Supplementary Information (SI) for Energy & Environmental Science.

Electronic Supplementary Information for

Accelerating lattice oxygen kinetics of layered oxide cathodes *via* active facet modulation and robust mechanochemical interface construction for high-energy-density sodium-ion batteries

Zhuang-Chun Jian,[ab] Wenjun Shi,[c] Yifeng Liu,[b] Xueyan Li,[d] Jiayang Li,[b] Yan-Fang Zhu,*[ab] Xu Zhu,[e] Yongchun Li,[f] Peng Tan,[d] Peng-Fei Wang,[e] Shuangqiang Chen,*[ab] Shilin Zhang,[g] Jianfeng Mao,[g] Guangmin Zhou,*[h] Xiaodong Guo,[i] Jiazhao Wang,[b] Shi-Xue Dou,[j] and Yao Xiao*[ab]

[a] College of Chemistry and Materials Engineering, Wenzhou University, Wenzhou, 325035, P. R. China. E-mail: yanfangzhu@wzu.edu.cn; chensq@wzu.edu.cn; xiaoyao@wzu.edu.cn

[b] Zhejiang Provincial Key Laboratory of Advanced Battery Materials and Technology, Wenzhou University Technology Innovation Institute for Carbon Neutralization, Wenzhou, Zhejiang 325035, P. R. China

[c] Department of Materials Science and Engineering, Southern University of Science and Technology, Shen Zhen, 518055, P. R. China

[d] Department of Thermal Science and Energy Engineering, University of Science and Technology of China, Hefei, 230026, P. R. China

[e] Center of Nanomaterials for Renewable Energy, State Key Laboratory of Electrical Insulation and Power Equipment, School of Electrical Engineering, Xi'an Jiaotong University, Xi'an, 710049, P.R. China

[f] Ångström Laboratory, Department of Chemistry, Uppsala University, SE 751 21 Uppsala, Sweden

[g] School of Chemical Engineering & Advanced Materials, University of Adelaide, Adelaide, SA 5005, Australia

[h] Tsinghua-Berkeley Shenzhen Institute & Tsinghua Shenzhen, International Graduate School, Tsinghua University, Shenzhen 518055, P. R. China. E-mail: guangminzhou@sz.tsinghua.edu.cn

[i] College of Chemical Engineering, Sichuan University, Chengdu 610065, P. R. China

[j] Institute of Energy Materials Science (IEMS), University of Shanghai for Science and Technology, Shanghai, 200093, China

This PDF file includes:

Materials and Methods

Materials synthesis

Air exposure experiments

Materials characterization

Electrochemical measurements

Numerical modeling

Results and Discussion

Figures S1 to S51

Tables S1 to S8

Notes S1 to S2

Equation S1

References

Materials and Methods

Materials synthesis.

The P2-$Na_{0.75}Li_{0.25}Mn_{0.75}O_2$ cathode material was prepared using a high-temperature solid-state reaction method. High-purity precursor materials, including Na_2CO_3 (99.9 %, Aladdin Co., Ltd.), LiOH (99.9 %, Aladdin Co., Ltd.), and MnO_2 (99.9 %, Aladdin Co., Ltd.), were weighed according to the stoichiometric ratio (with a 2 % overdose of Na_2CO_3 and LiOH to compensate for volatilization during high-temperature calcination). The precursors were thoroughly ground in an agate mortar for 45 minutes to ensure homogeneity. After the material has been ground well, the powder is transferred to a tablet press and compacted into flakes under a pressure of 16 MPa. The compacted material was then transferred to a muffle furnace and roasted in an air atmosphere at a temperature of 700 °C for 15 hours, finally cooling down naturally to room temperature to obtain a substrate material.

The P2-$Na_{0.75}Li_{0.25}Mn_{0.75}O_2$@x%mol $Na_{0.44}MnO_2$ (x=0, 5, 10, 15) cathode material was prepared using the liquid phase method. Precisely weighed CH_3COONa and Mn $(CH_3COO)_2\cdot 4H_2O$ were dissolved in ethanol under magnetic stirring at 60 °C for 30 minutes to ensure complete dissolution. Then the P2-$Na_{0.75}Li_{0.25}Mn_{0.75}O_2$ positive electrode material is added to the solution and stirred rapidly for about 15−20 minutes to ensure that the P2-$Na_{0.75}Li_{0.25}Mn_{0.75}O_2$ positive electrode material is evenly distributed in the solution. The required amount of oxalic acid solution (solvent is ethanol) is added dropwise to the solution and stirring is continued for 60 minutes to ensure that the resulting $Na_2C_2O_4$ and MnC_2O_4 precipitates are fully covered on the surface of the P2-$Na_{0.75}Li_{0.25}Mn_{0.75}O_2$ cathode material. The solution was later placed in a blast oven at 120 °C to evaporate the solution for 6 hours. The resulting powder was then transferred to a muffle furnace and sintered in an air atmosphere at a temperature of 800 °C for 8 hours and left to cool down naturally to around 100−150 °C. The resulting materials were transferred promptly to an Argon filled glove box (H_2O and O_2 < 0.1 ppm) to avoid moisture absorption.

Air exposure experiments.

For the air stability evaluation, the synthesized P2-$Na_{0.75}Li_{0.25}Mn_{0.75}O_2$ (NLMO) and P2-$Na_{0.75}Li_{0.25}Mn_{0.75}O_2$@10 %mol $Na_{0.44}MnO_2$ (NLMO-T10) cathode materials were divided into six aliquots (each weighing approximately 300 mg) and sealed in individual glass vials equipped with desiccant plugs. These samples were exposed to ambient air at room temperature (25–26 °C, relative humidity approximately 45–50 %) for varying durations of 1, 3, 5, and 7 days. After each designated exposure period, the samples were immediately labeled, hermetically sealed, and subjected to comprehensive characterization, including X-ray diffraction (XRD), scanning electron microscopy (SEM), and electrochemical performance testing. The evolution of structural integrity and electrochemical behavior under air exposure was systematically analyzed to evaluate the impact of surface reactivity on material stability.

Materials characterization.

Powder X-ray diffraction (**XRD**) patterns were collected on a PANalytical Aeris X-ray diffractometer with Cu Kα radiation source (λ = 1.5406 Å) at a scanning rate of 2° $\min^{-1}$. The lattice parameters were refined by FullProf software based on the Rietveld method. The CIF card of the standard P2 phase mode *($P6_3/mmc$* space group) and raw data were imported into FullProf. The experimental parameters, peak shape parameters and structural parameters were adjusted by the least squares method, and then the calculated peak shape and the experimental peak shape were fitted to maximum agreement. Finally, the cell parameters and other information/parameters were obtained. The morphological and structural peculiarities were characterized by scanning electron microscopy (**SEM**, SEM3100, CIQTEK Co., Ltd.) and transmission electron microscopy (**TEM**, JEOL JEM-2011, Limited Corporation, Japan, 200 kV), respectively. High angle annular dark field-scanning transmission electron microscopy (**HAADF-STEM**) and annular-bright field-scanning transmission electron microscopy (**ABF-STEM**) were performed on a JEM-ARM300F2. The X-ray absorption fine structure (**XAFS**) spectra of Mn *K*-edge for powder samples were collected in transmission mode on a commercial Laboratory-Based XAFS spectrometer (Table XAFS-500A, Specreation Instruments Co., Ltd.). An X-ray tube was used to generate X-ray, and the voltage and current were set to 20 kV and 15 mA. The Ge (531) spherically bent crystal analyzers with a radius of curvature of 500 mm and the R250 mm Rowland circle were used to provide monochromatized X-ray beam. We thank Specreation Instruments Co., Ltd. for XAFS measurements and related analysis. X-ray photoelectron spectroscopy (**XPS**) characterization was carried out on a Thermo Scientific Nexsa X-ray photoelectron spectrometer. Synchrotron radiation *ex-situ* X-ray absorption spectroscopy (***ex-situ* XAS**) measurements were conducted at the wiggler XAS Beamline (12ID) at the Australian Synchrotron in Melbourne, by using a set of liquid N_2 cooled Si (311) monochromator crystals. The ATHENA software was used to analyze the XAS data. The soft-XAS **(sXAS)** spectra in PFY modes were first normalized to the incident beam intensity and subsequently to the pre-and post-edge absorption levels. ***In-situ* synchrotron-based XRD** tests for NLMO cathode materials were carried out at Australian Synchrotron, Melbourne, Australia, using the LaB_6 NIST standard reference material 660b. ***In-situ* charge and discharge XRD** tests for NLMO-T10 cathode materials were collected between 2θ = 10° and 80° at 0.1 C by using a special Swagelok cell with an ultra-thin aluminum window for X-ray window for penetration. The **Zeta electric potential** was tested on Nanoparticle Analyzer (nanoPartica SZ-100-S2, HORIBA scientific Ltd, Japan). The Resonant inelastic X-ray scattering (**RIXS**) experiments were conducted at beamline U41-PEAXIS at BESSY II, located at Helmholtz-Zentrum Berlin (HZB). A vacuum suitcase was used to transfer the sample from an N_2-filled glovebox to the test chamber. The spectrometer was positioned at specular conditions relative to 60° scattering angle and was optimized to a combined resolution of 90 meV using a copper tape. The O *K*-edge RIXS spectra of the samples were collected at an excitation energy of 531.0 eV. The acquisition time for each pattern was 20 min. Electron Paramagnetic Resonance (**EPR**) testing was conducted using a high-sensitivity EPR spectrometer (EMXplus, Bruker Corporation, Germany). The sample was placed in a quartz sample tube and subjected to an external magnetic field at room temperature under vacuum conditions. An internal microwave resonant cavity and a superconducting magnet to apply an external magnetic field to the sample. The resonance absorption signals of unpaired electrons in the sample under the influence of the magnetic field were recorded using a high-sensitivity detector. *In-situ* Differential Electrochemical Mass Spectrometry (***in-situ*** **DEMS**) testing was conducted using a high-sensitivity electrochemical mass spectrometry system (HPR-40, Hiden Analytical Ltd, UK). During the experiment, the electrochemical samples to be tested were placed in a specially designed electrochemical cell. Under constant temperature and constant current conditions, the gaseous products generated by the reaction were continuously transferred to the high-vacuum detection chamber of the mass spectrometer through a microporous membrane. The ion current signals at different mass-to-charge ratios (m/z) were recorded using a high-sensitivity Faraday cup detector.

Electrochemical measurements.

The Na^+ storage performance of P2-$Na_{0.75}Li_{0.25}Mn_{0.75}O_2$@x %mol $Na_{0.44}MnO_2$ (x = 0, 5, 10, 15) cathode materials was evaluated in CR2032 coin cells (Canrd Technology Co., Ltd.) which assembled in an Ar-filled glove box (H_2O, $O_2 < 0.1$ ppm). The positive electrodes were prepared by mixing 70 wt% of active material, 20 wt% of Super P carbon, and 10 wt% of polyvinylidene difluoride (PVDF) binder in N-methyl-2-pyrrolidone (NMP) to obtain a slurry, then pouring it onto carbonized Al foil, followed by vacuum drying at 80 °C overnight. The mass loading of active material in each electrode pellet (10.0 mm in diameter) was about 2–3 mg cm^{-2}. For half-cell system, metallic sodium, porous glass fibers, and 100 µl of 1.0 M $NaClO_4$ dissolved in propylene carbonate (PC) with 5 vol% fluoroethylene carbonate (FEC) additive were separately used as counter electrode, separator, and electrolyte. The assembled coin cells were tested by galvanostatic charged/discharge (GCD) cycling on a Neware battery test system (CT-4008, Shenzhen, China) in the voltage range of 1.5−4.4 V versus Na^+/Na. Cyclic voltammetry (CV) and galvanostatic intermittent titration technique (GITT) measurements were performed on a Princeton instruments testing system. For the GITT test, the batteries were charged at 0.1 C for 30 min, followed by a relaxation process under open circuit relaxation for 10 h with potential windows of 1.5−4.4 V.

Numerical modeling.

To investigate the stress evolution in the NLMO-T10 cathode material during electrochemical cycling, a numerical modeling approach was employed to simulate the coupled processes of sodium diffusion and mechanical stress generation. The kinetics of sodium diffusion in the NLMO-T10 cathode materials is governed by the *Fick*'s law, $dC/dt = D\nabla^2C$, where C is the concentration of sodium concentration in the cathode materials, and D is the diffusivity of sodium that is dependent on the grain orientation. We assume the diffusion of sodium within the *a-b* plane (*i.e.,* $D_{a\text{-}b} = 1\times10^{-10}$ cm^2/s) is faster than that along the *c* direction (*i.e.,* $D_c = 1\times10^{-11}$ cm^2/s). A uniform sodium flux was applied to the surface of the cathode particle, with its magnitude determined based on the C-rate (*i.e.,* 0.5 C). The strain field induced by sodium insertion and extraction was derived from the evolution of lattice parameters observed in situ XRD patterns during charging. The stress field was subsequently computed within the framework of linear elasticity theory, considering the material properties of NLMO-T10, including the Young's modulus of 100 GPa and the Poisson's ratio of 0.5. The governing equations were solved using COMSOL Multiphysics software, integrating electrochemical and mechanics modules. This enabled the simulation of sodium ion diffusion, strain field evolution, and stress distribution during cycling. The results were validated against experimental observations, providing insights into the relationship between sodium transport and mechanical stability of NLMO-T10.

Results and Discussion

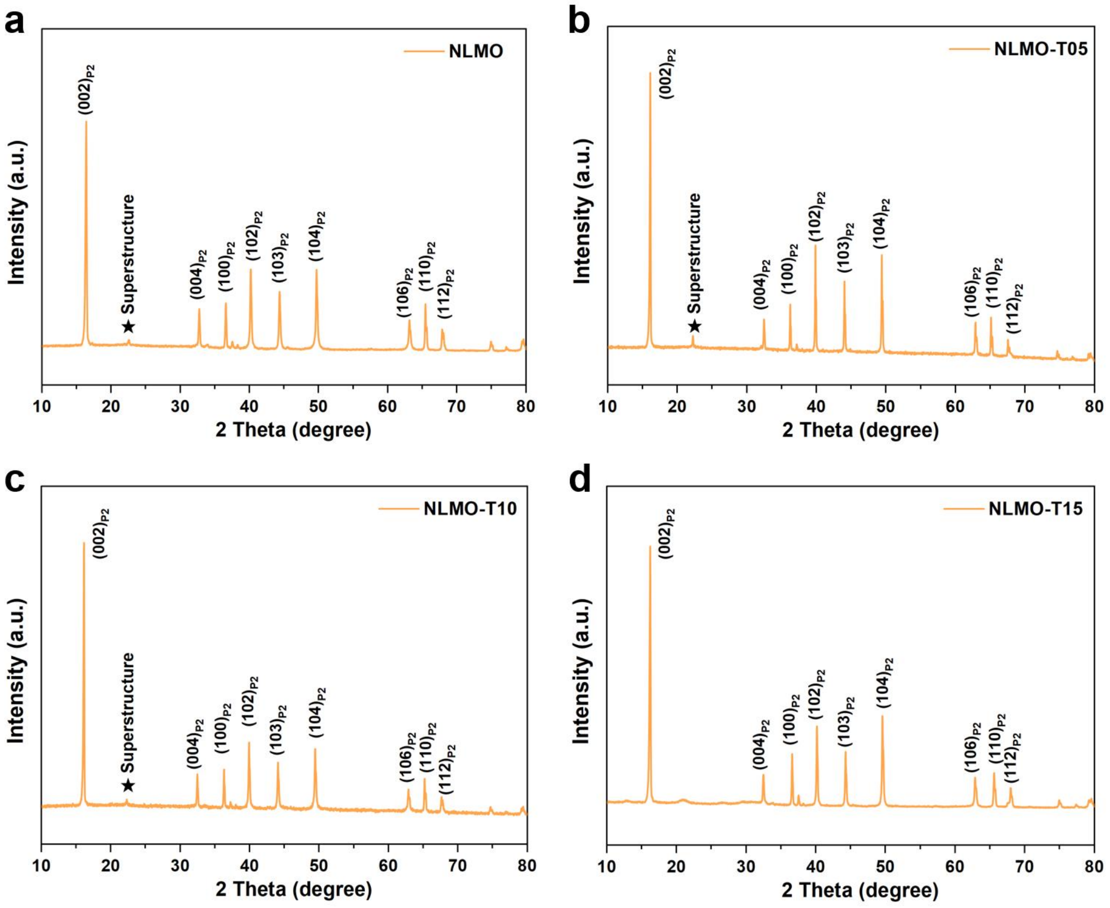

Figure S1. Powder XRD patterns of a) NLMO, b) NLMO-T05, c) NLMO-T10 and d) NLMO-T15. The superstructure diffraction peak at 21−22.5° could signify the honeycomb ordering of Li and Mn.

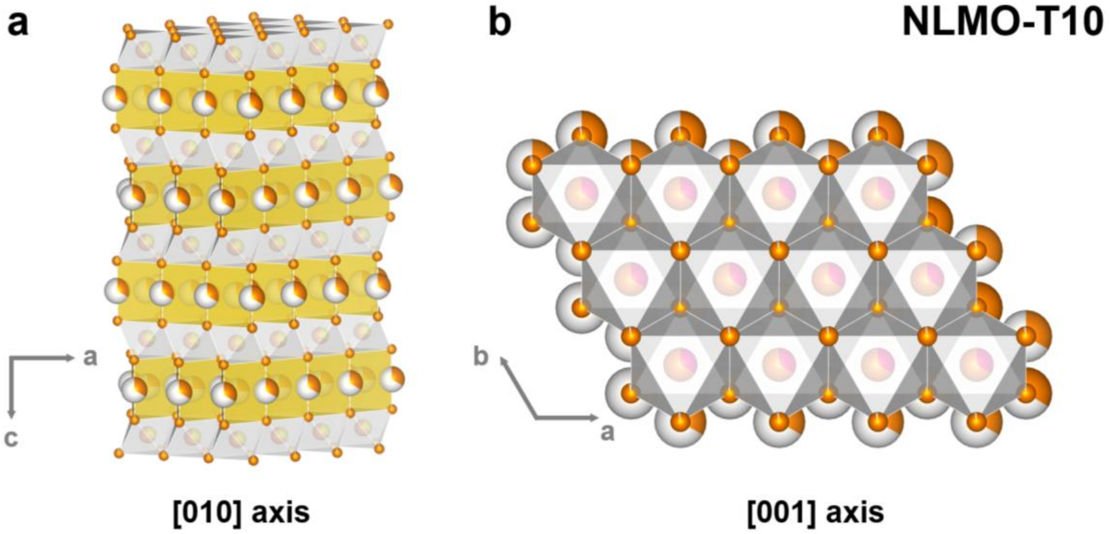

Figure S2. P2-type bulk structure along a) [010] and b) [001] axis in NLMO-T10.

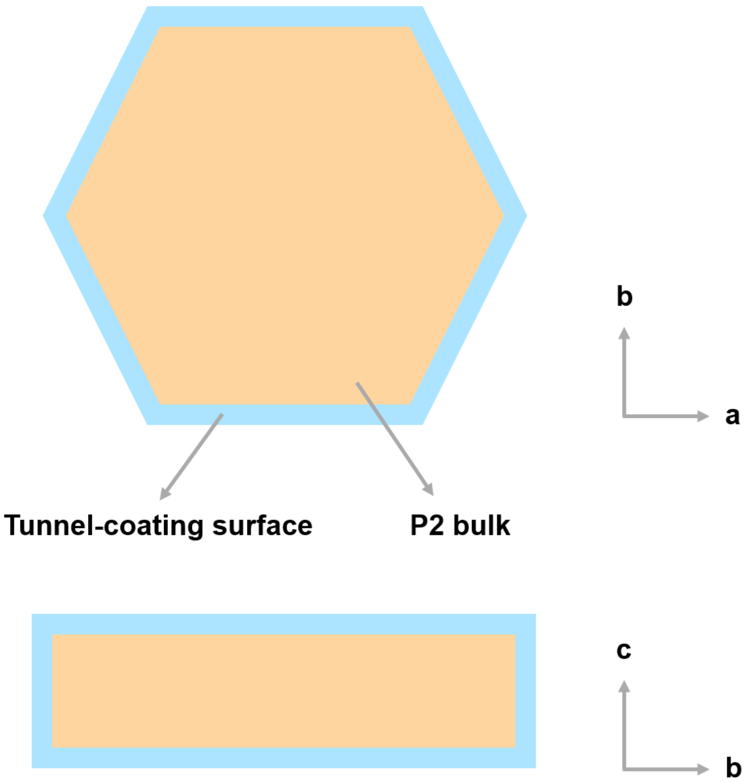

Figure S3. Schematic diagram of the cross section of hierarchical crystalline domain for NLMO-T10.

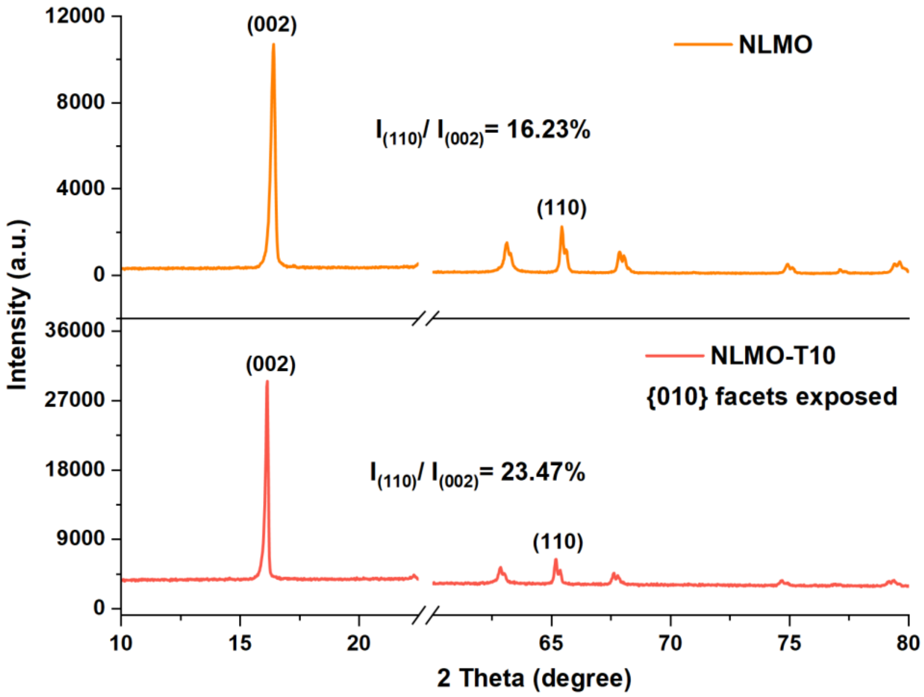

Figure S4. I $_{(110)}$/ I $_{(002)}$ values calculated from XRD patterns of NLMO and NLMO-T10.

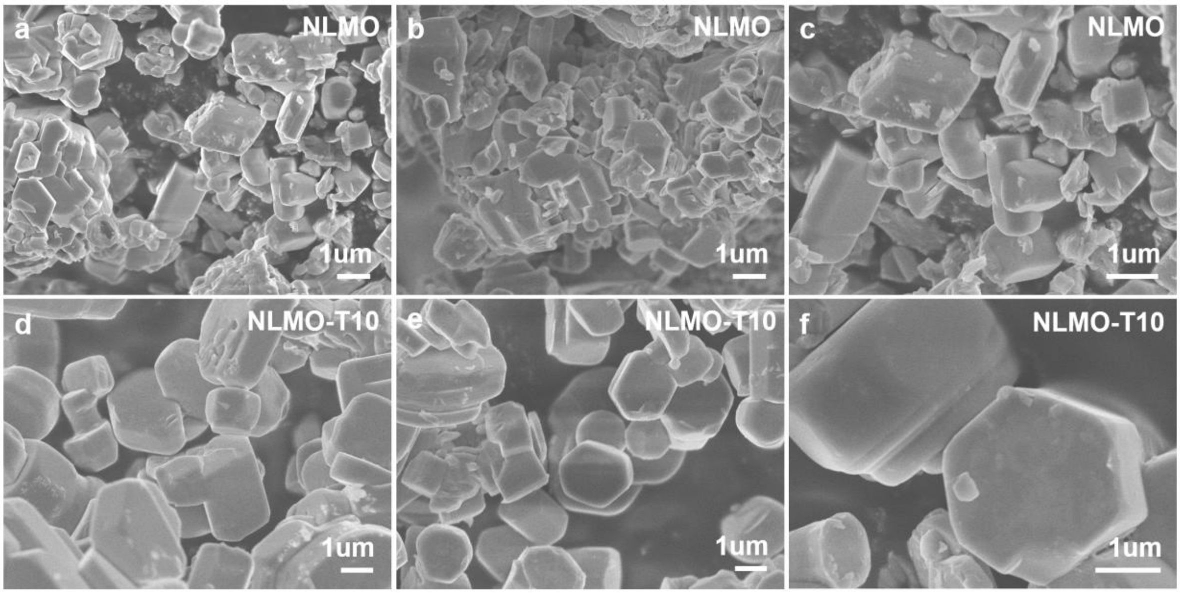

Figure S5. SEM images of a-c) NLMO and d-f) NLMO-T10.

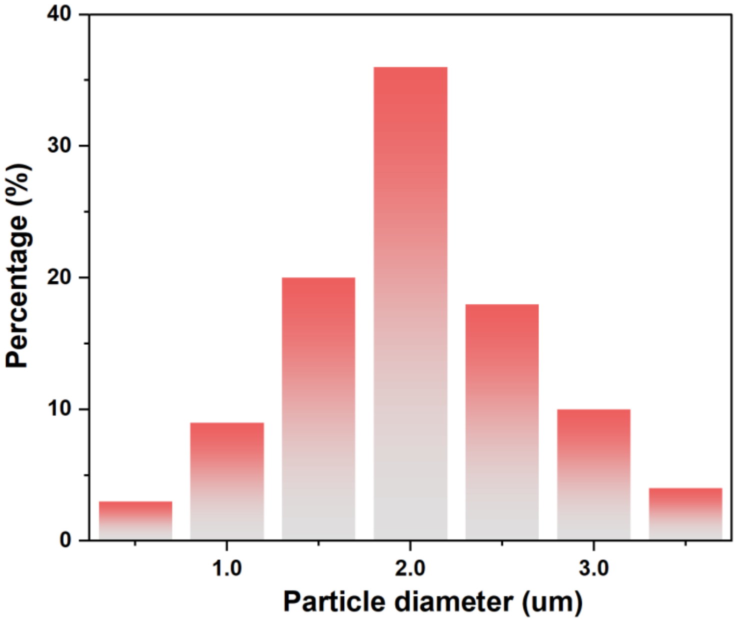

Figure S6. Particle diameter distribution of NLMO-T10.

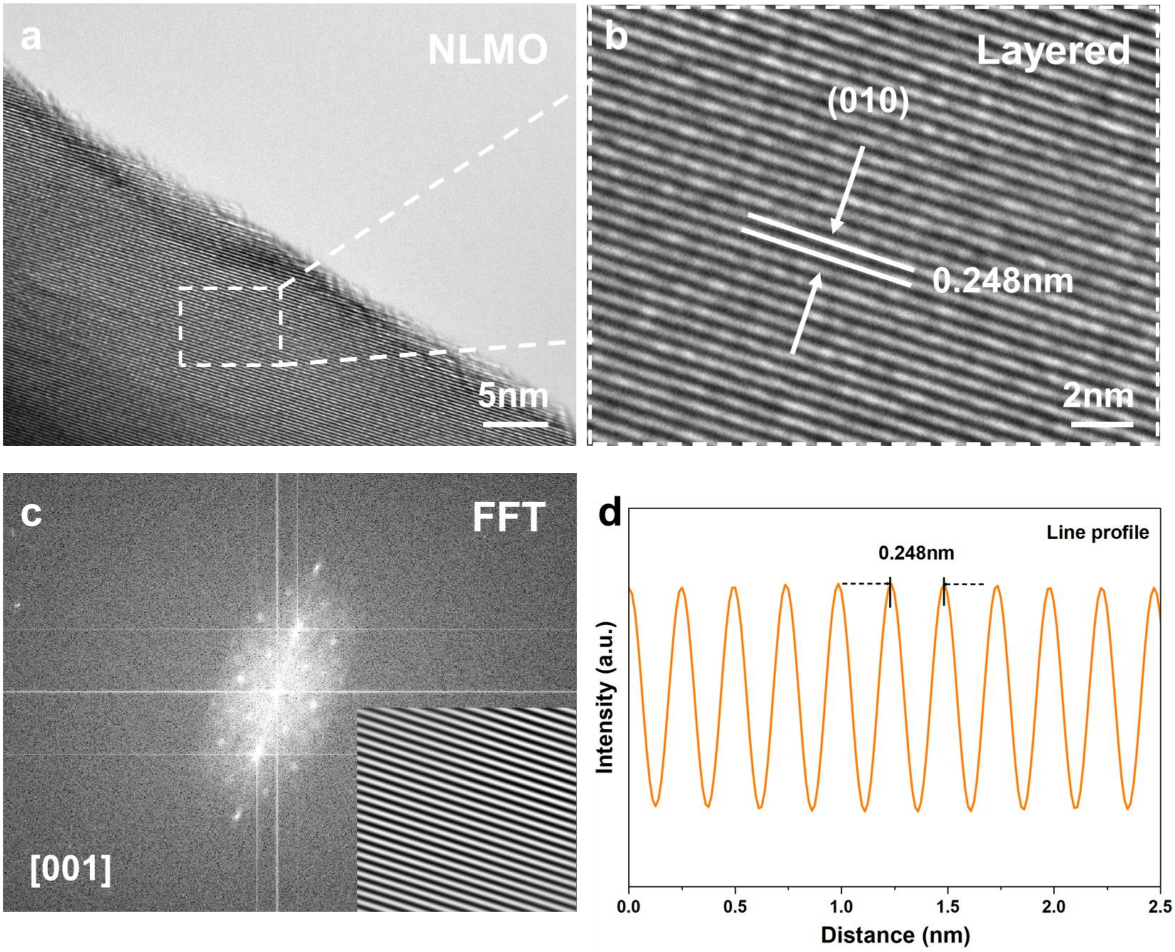

Figure S7. a) HR-TEM images of NLMO. b) Enlarged view of the white region marked in a). c) FFT image and d) Intensity line profile of NLMO.

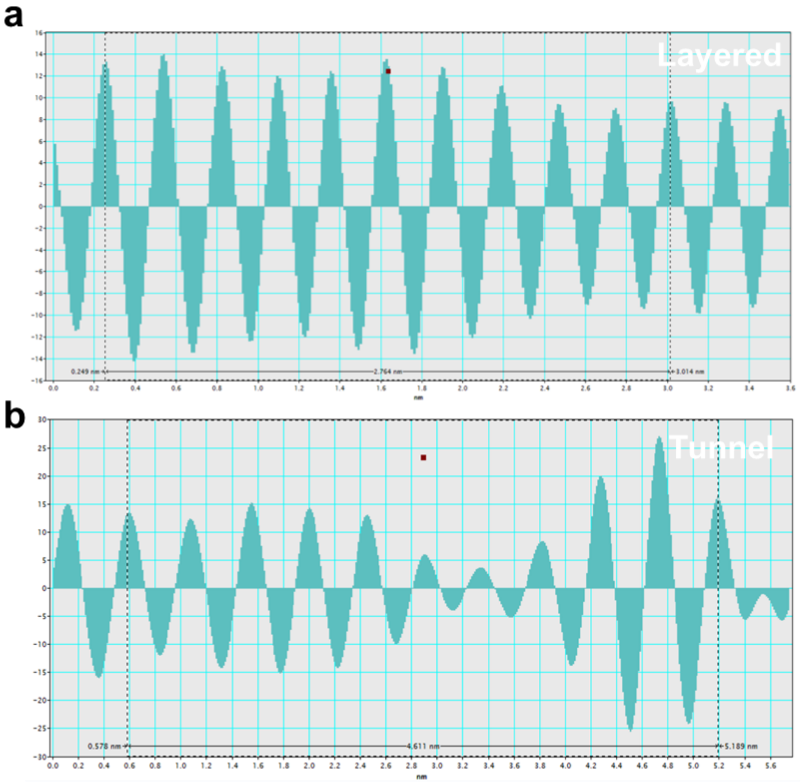

Figure S8. Line profiles of a) layered structure and b) tunnel structure of NLMO-T10.

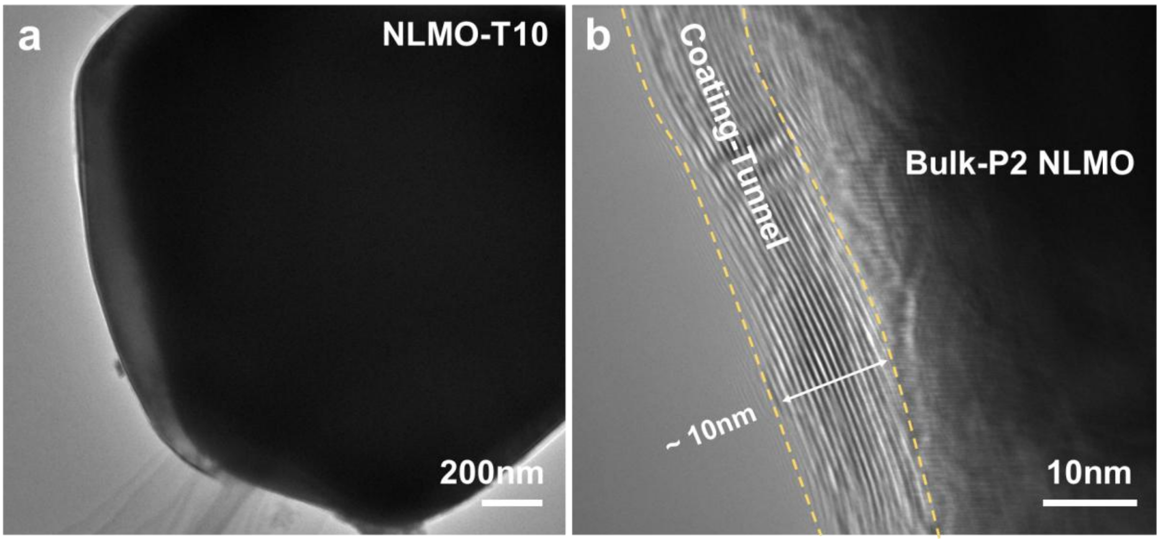

Figure S9. a-b) HR-TEM images of NLMO-T10.

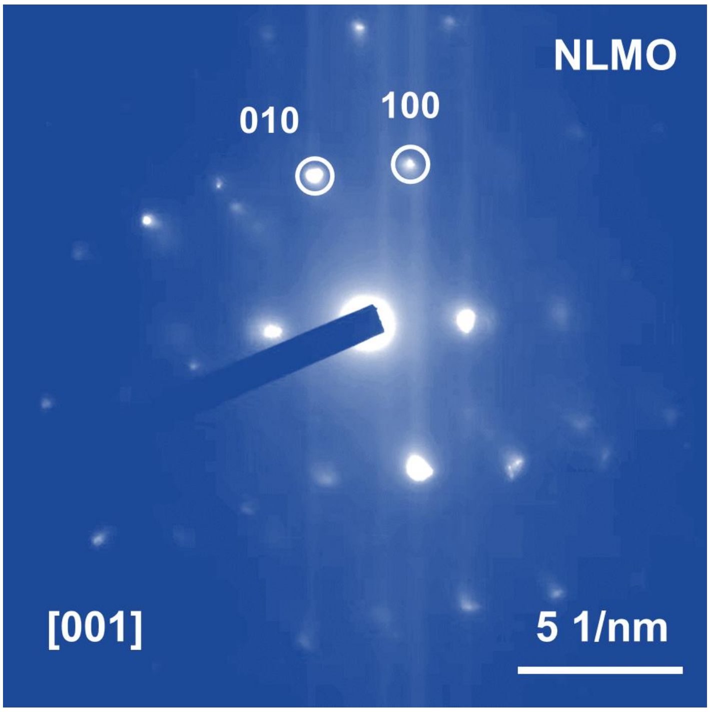

Figure S10. SAED patterns projected from the zone [001] axis of NLMO.

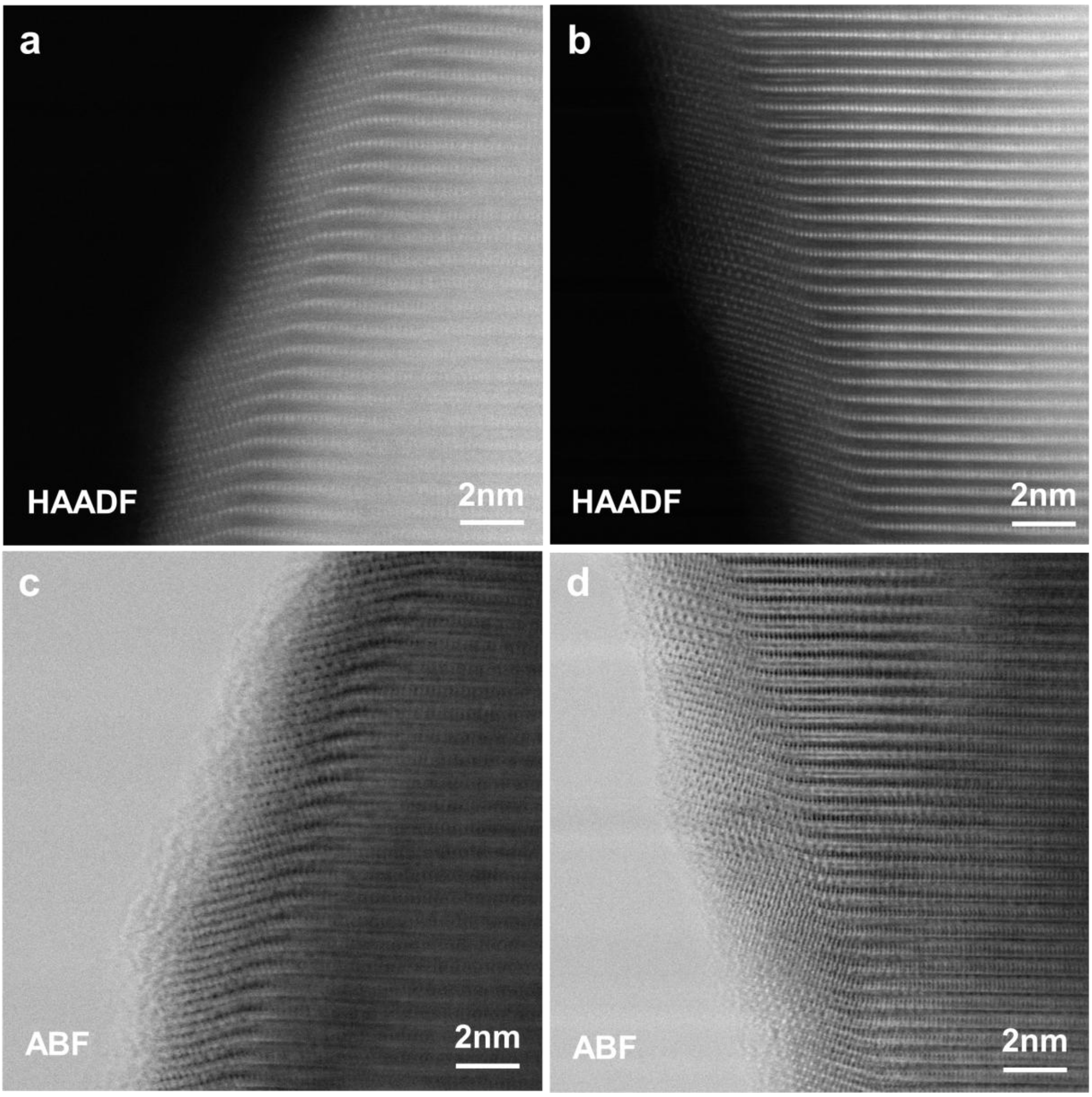

Figure S11. a, b) HAADF-STEM and c, d) ABF-STEM images of NLMO-T10.

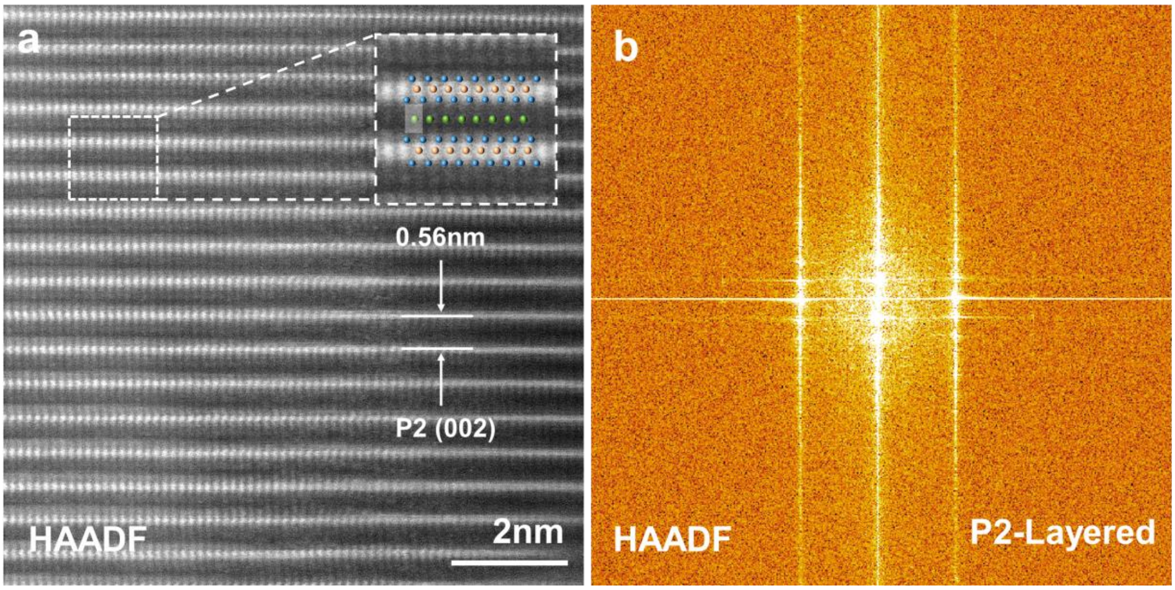

Figure S12. a) HAADF-STEM image and b) FFT image of HAADF-STEM of the P2-bulk in NLMO-T10.

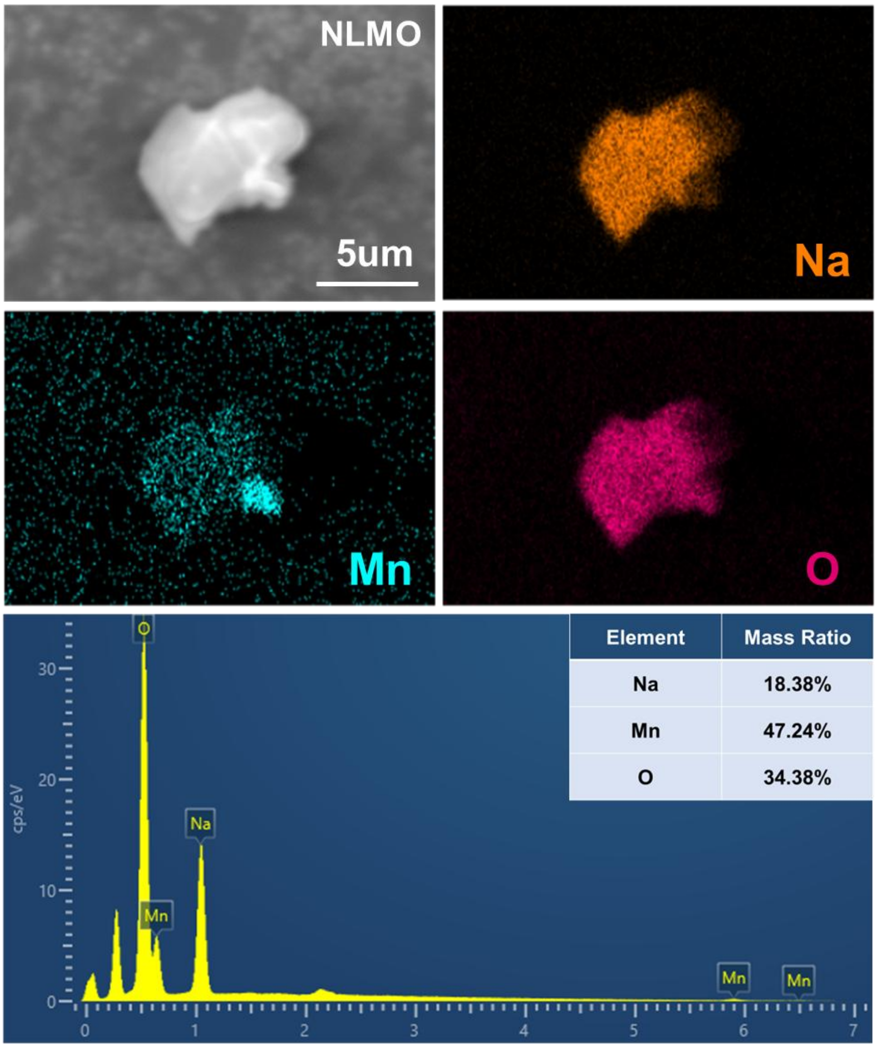

Element	Mass Ratio
Na	18.38%
Mn	47.24%
O	34.38%

Figure S13. SEM-EDS mapping images of NLMO.

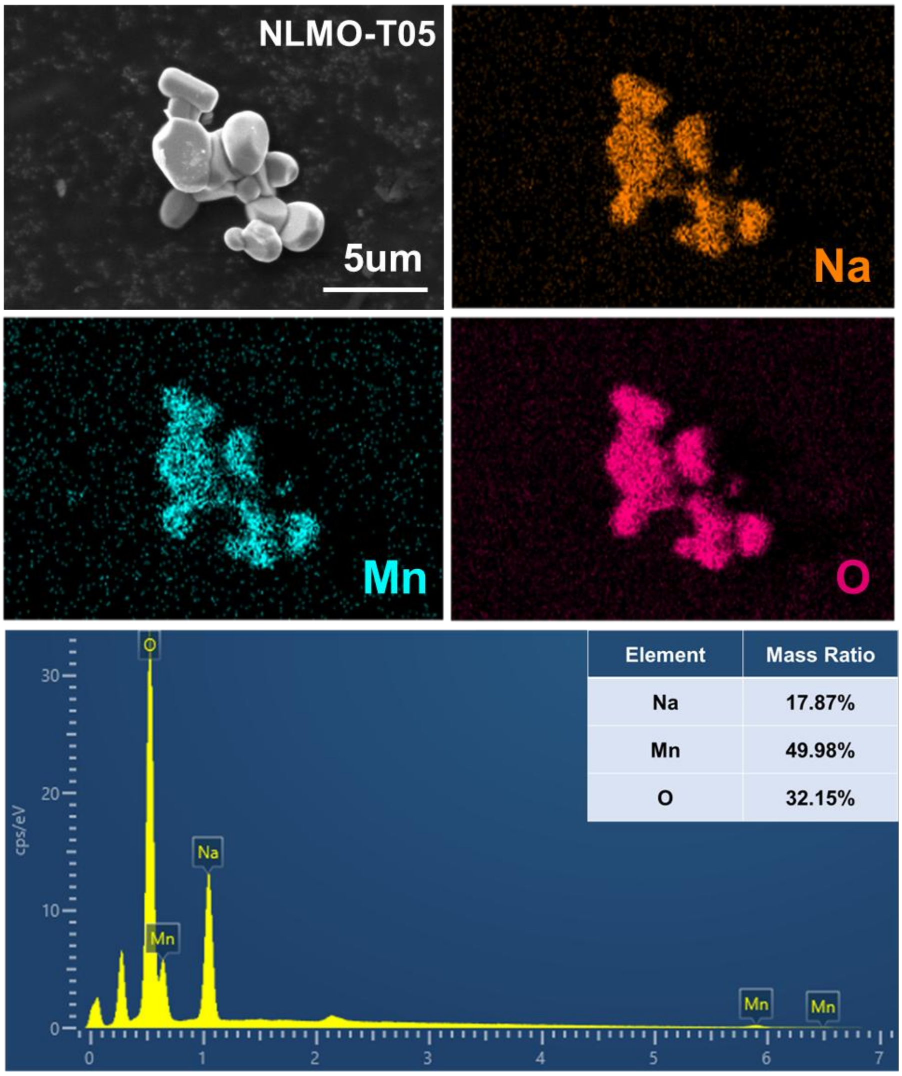

Element	Mass Ratio
Na	17.87%
Mn	49.98%
O	32.15%

Figure S14. SEM-EDS mapping images of NLMO-T05.

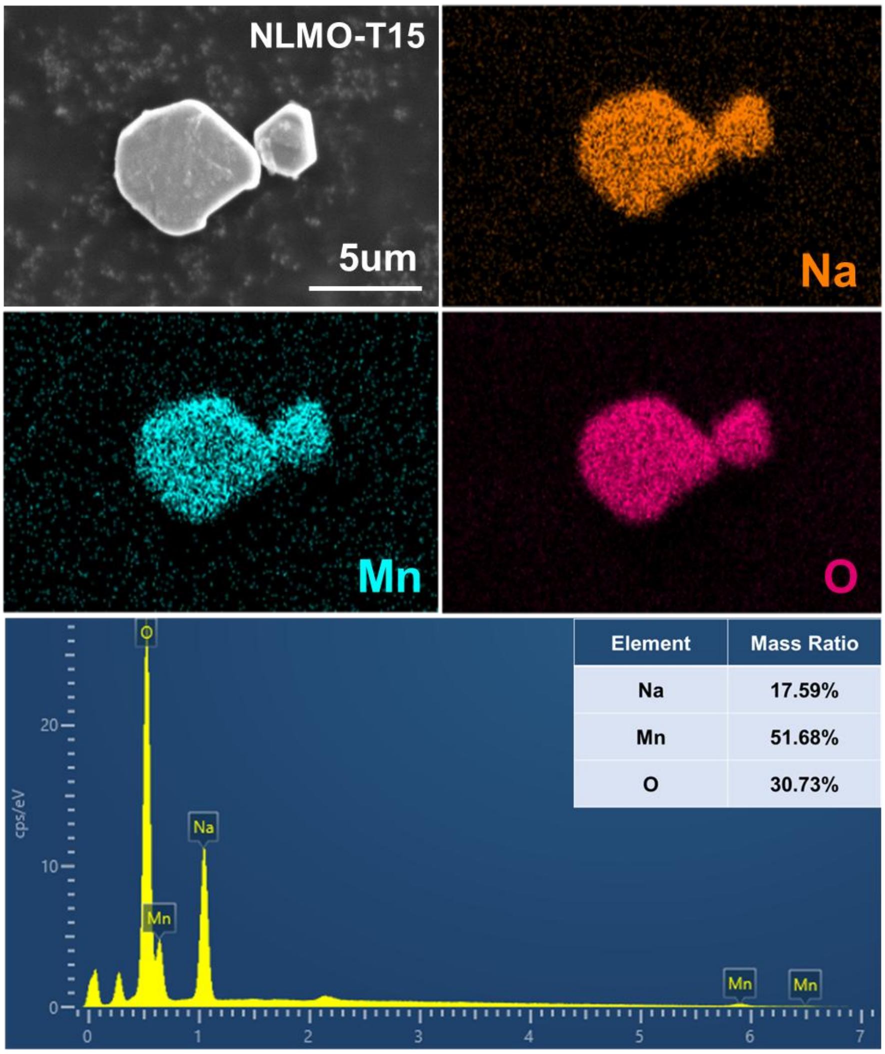

Element	Mass Ratio
Na	17.59%
Mn	51.68%
O	30.73%

Figure S15. SEM-EDS mapping images of NLMO-T15.

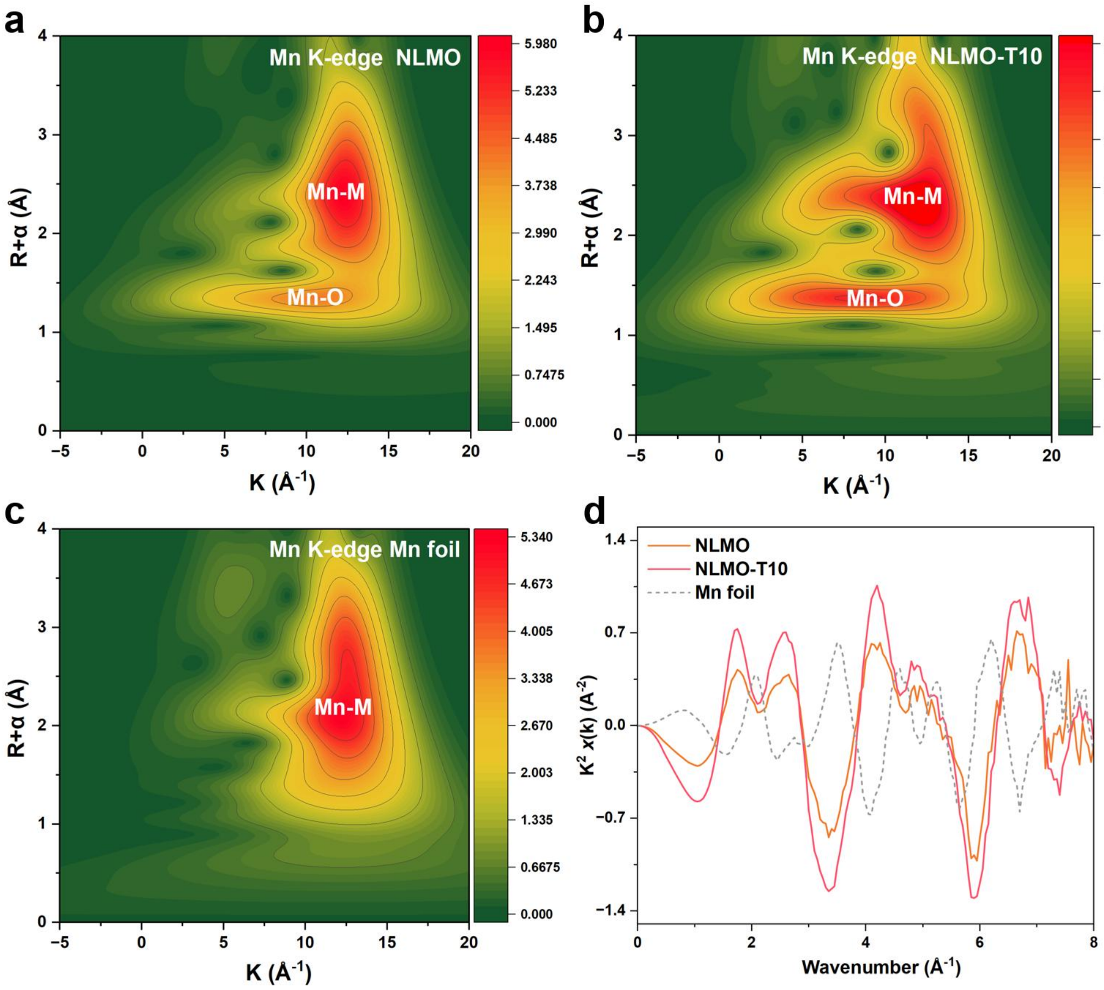

Figure S16. Contour plots of the Mn *K*-edge WT-EXAFS spectra of a) NLMO, b) NLMO-T10 and c) Mn foil. d) Mn *K*-edge k spaces EXAFS spectra of NLMO, NLMO-T10 and Mn foil.

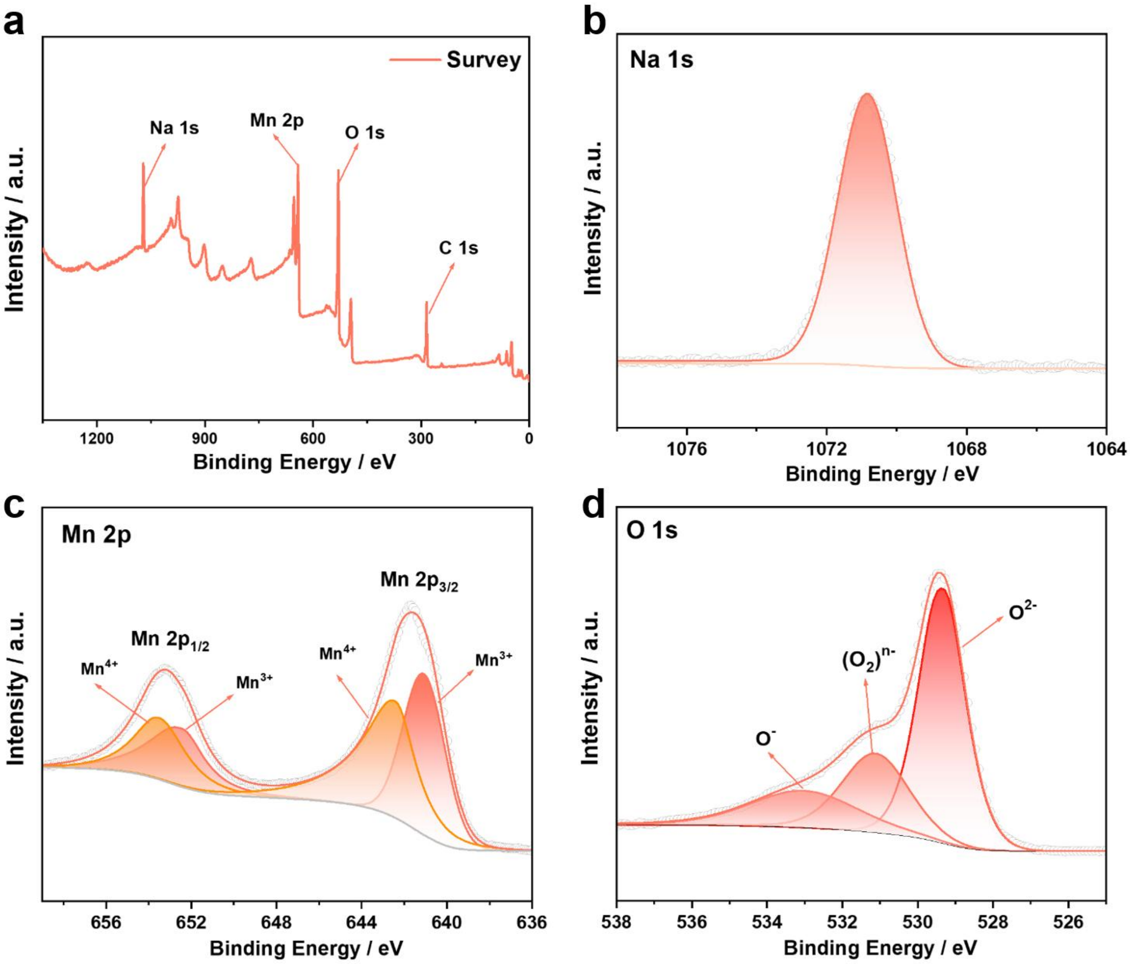

Figure S17. XPS spectrum of NLMO-T10 cathode materials' surface. a) survey spectrum, b) Na 1s, c) Mn 2p and d) O 1s.

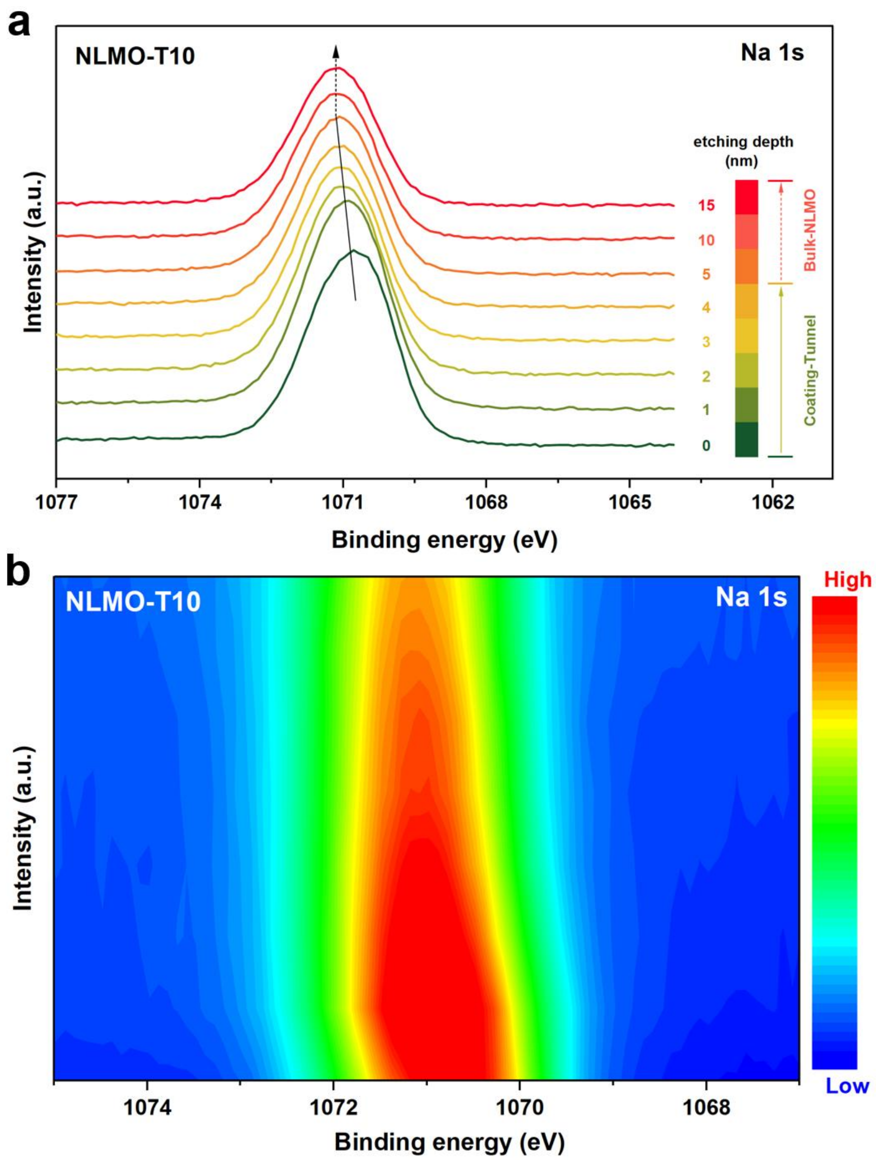

Figure S18. a, b) Na 1s XPS etching analysis of NLMO-T10.

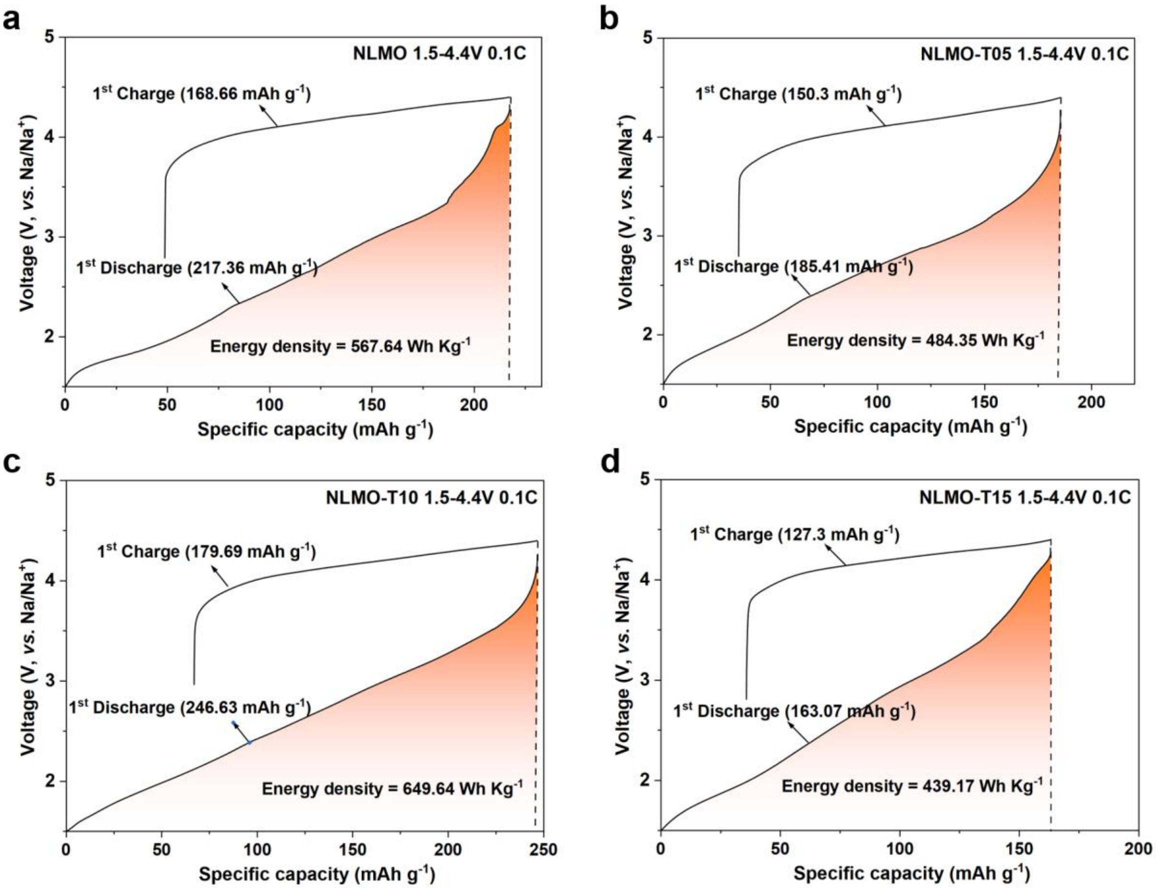

Figure S19. Initial GCD curves versus specific capacity and corresponding energy densities (shadow areas) of a) NLMO, b) NLMO-T05, c) NLMO-T10, d) NLMO-T15 electrodes in the voltage range of 1.5−4.4 V.

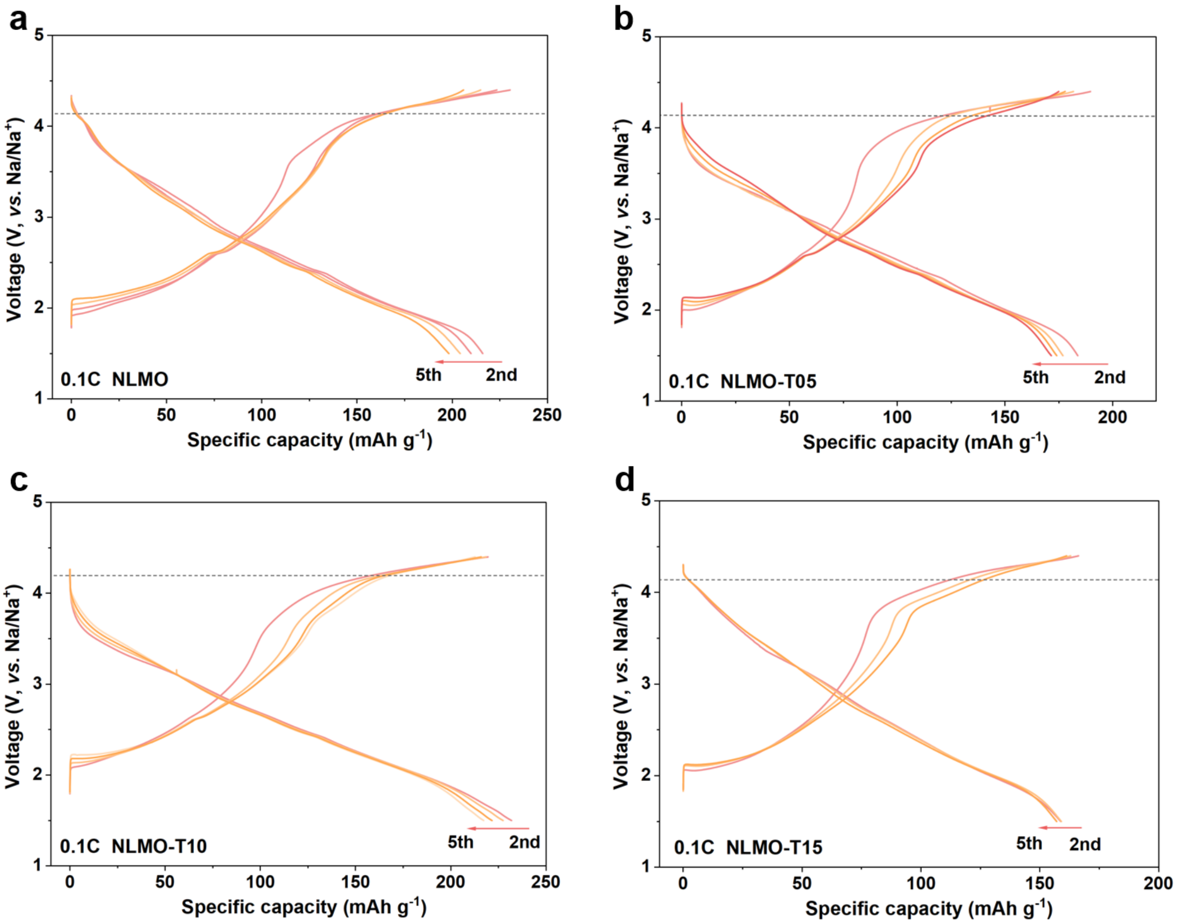

Figure S20. GCD curves versus specific capacity of a) NLMO, b) NLMO-T05, c) NLMO-T10, d) NLMO-T15 electrodes in 2nd, 3rd, 4th, 5th cycles at 0.1 C in the voltage range of 1.5−4.4 V.

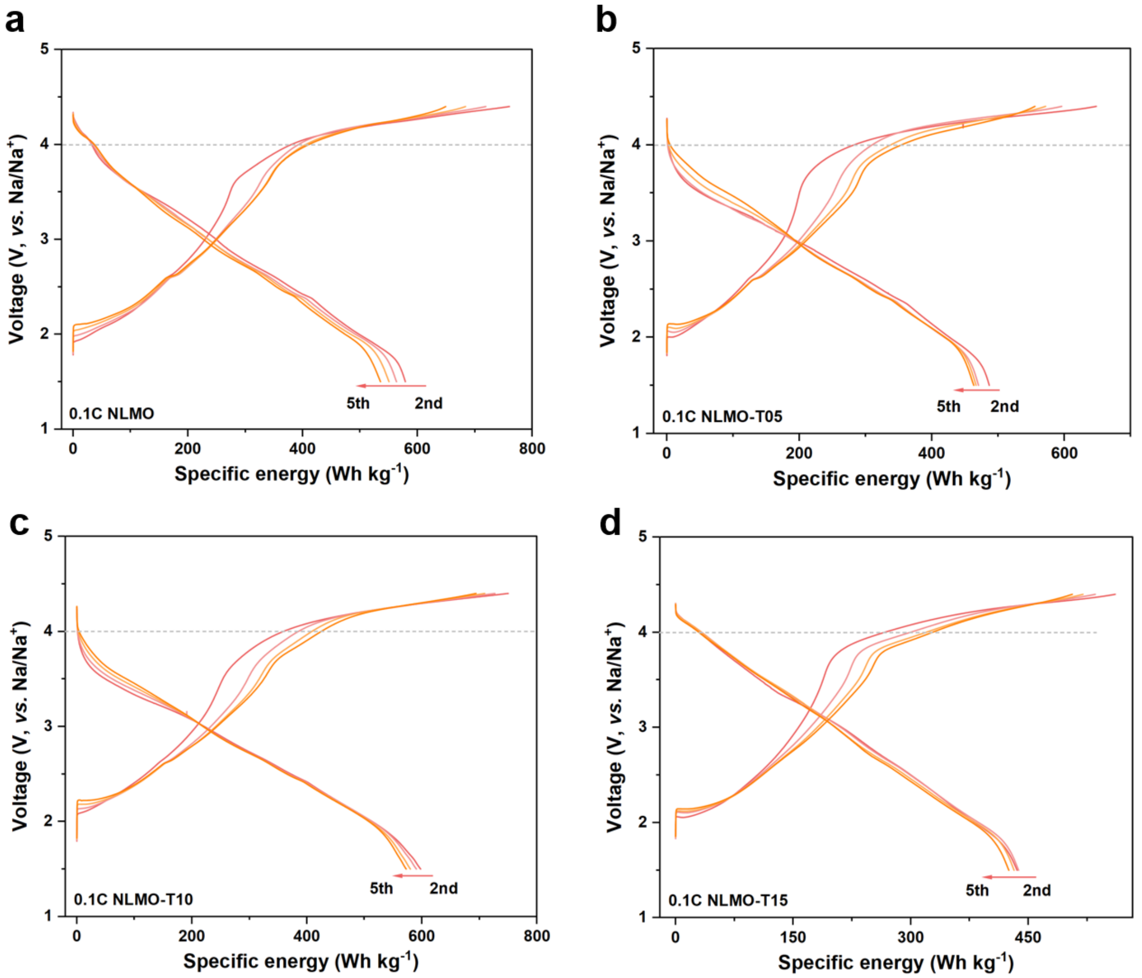

Figure S21. GCD curves versus specific energy of a) NLMO, b) NLMO-T05, c) NLMO-T10, d) NLMO-T15 electrodes in 2nd, 3rd, 4th, 5th cycles at 0.1 C in the voltage range of 1.5−4.4 V.

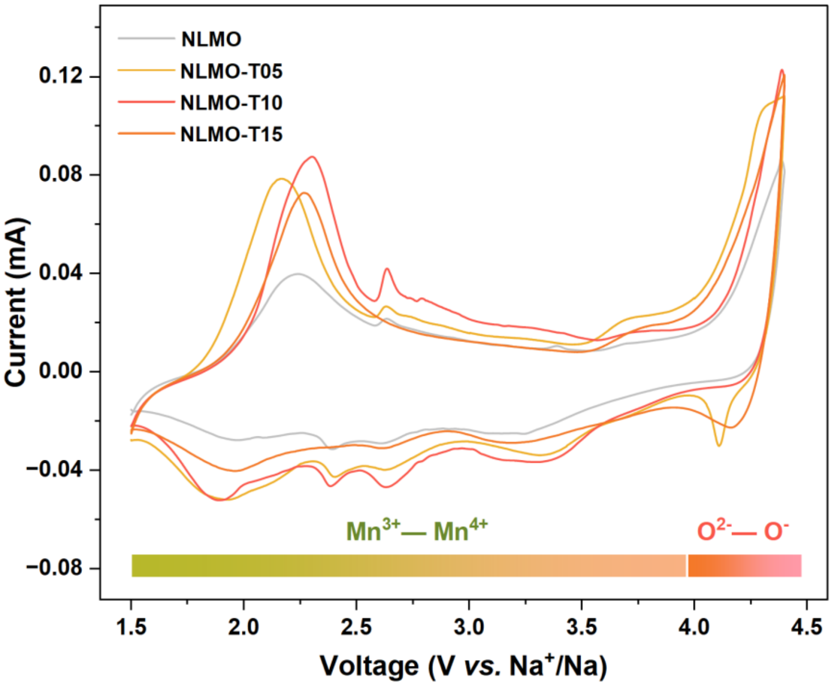

Figure S22. CV curves at 0.1 mV s^{-1} of NLMO, NLMO-T05, NLMO-T10 and NLMO-T15 electrodes in the voltage range of 1.5−4.4 V.

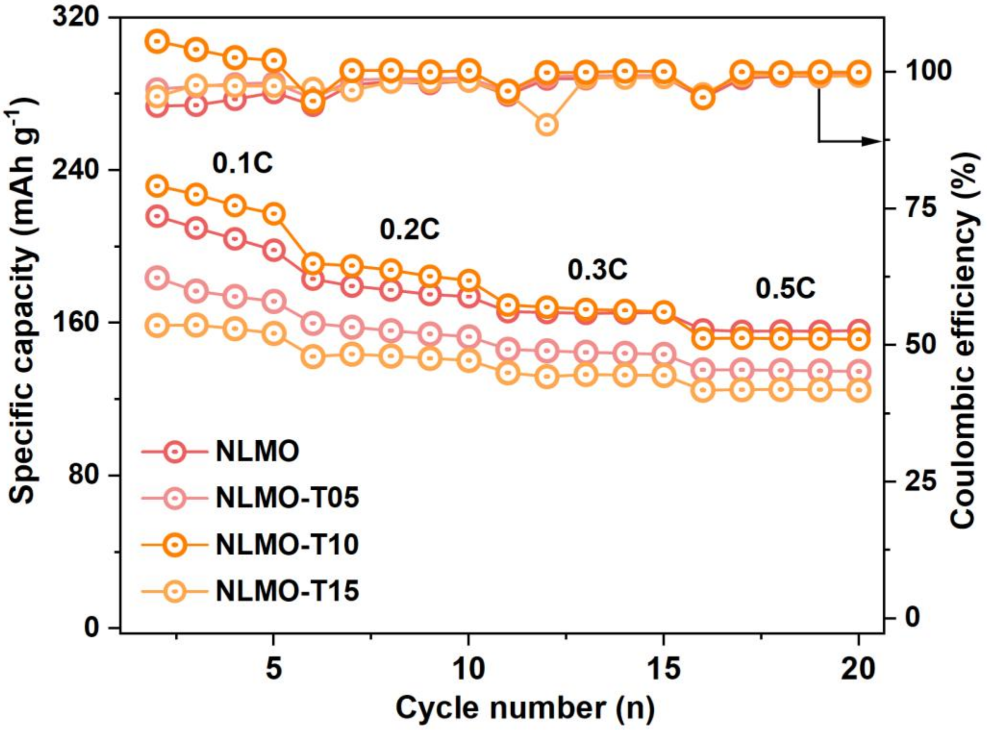

Figure S23. Rate performance of NLMO, NLMO-T05, NLMO-T10 and NLMO-T15 electrodes at various rates in the voltage range of 1.5−4.4 V.

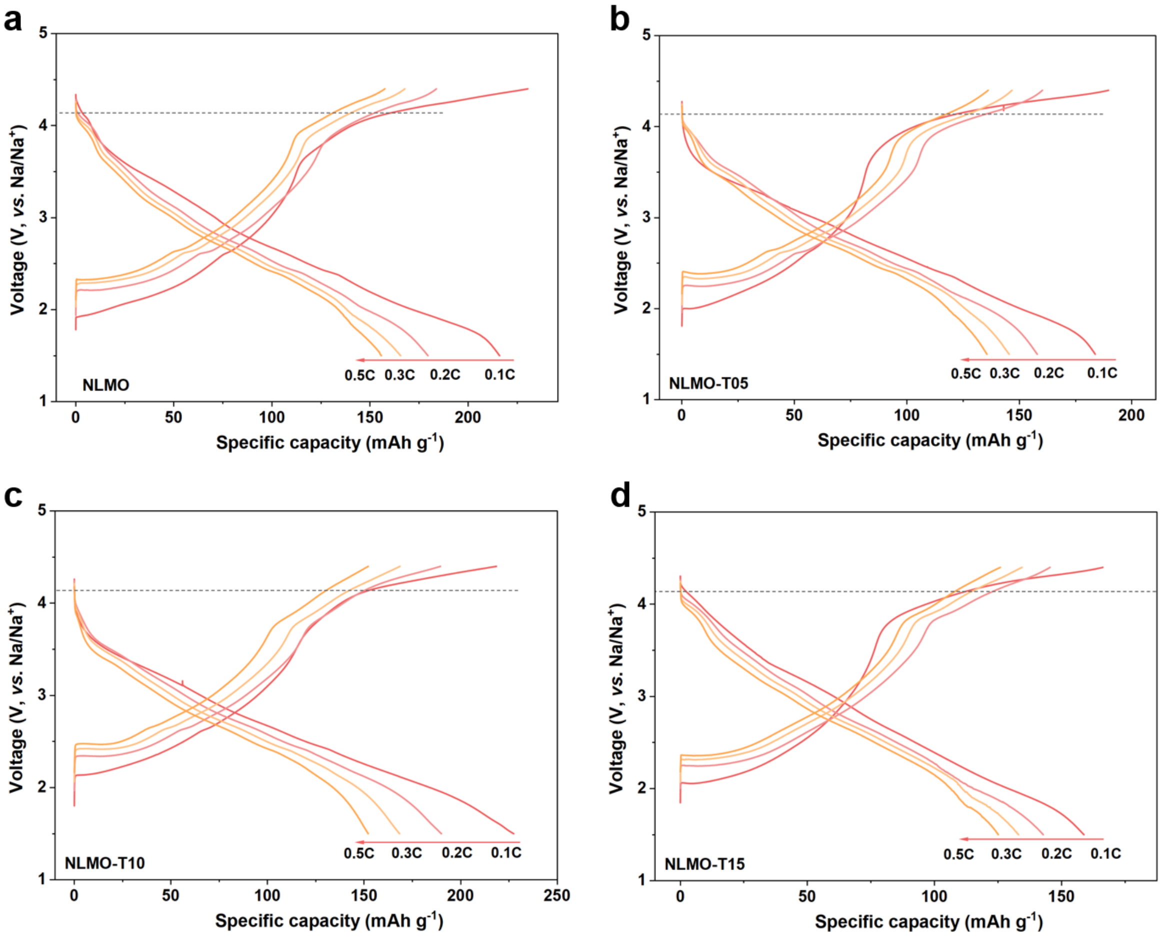

Figure S24. GCD curves versus specific capacity of a) NLMO, b) NLMO-T05, c) NLMO-T10, d) NLMO-T15 electrodes at various rates in the voltage range of 1.5−4.4 V.

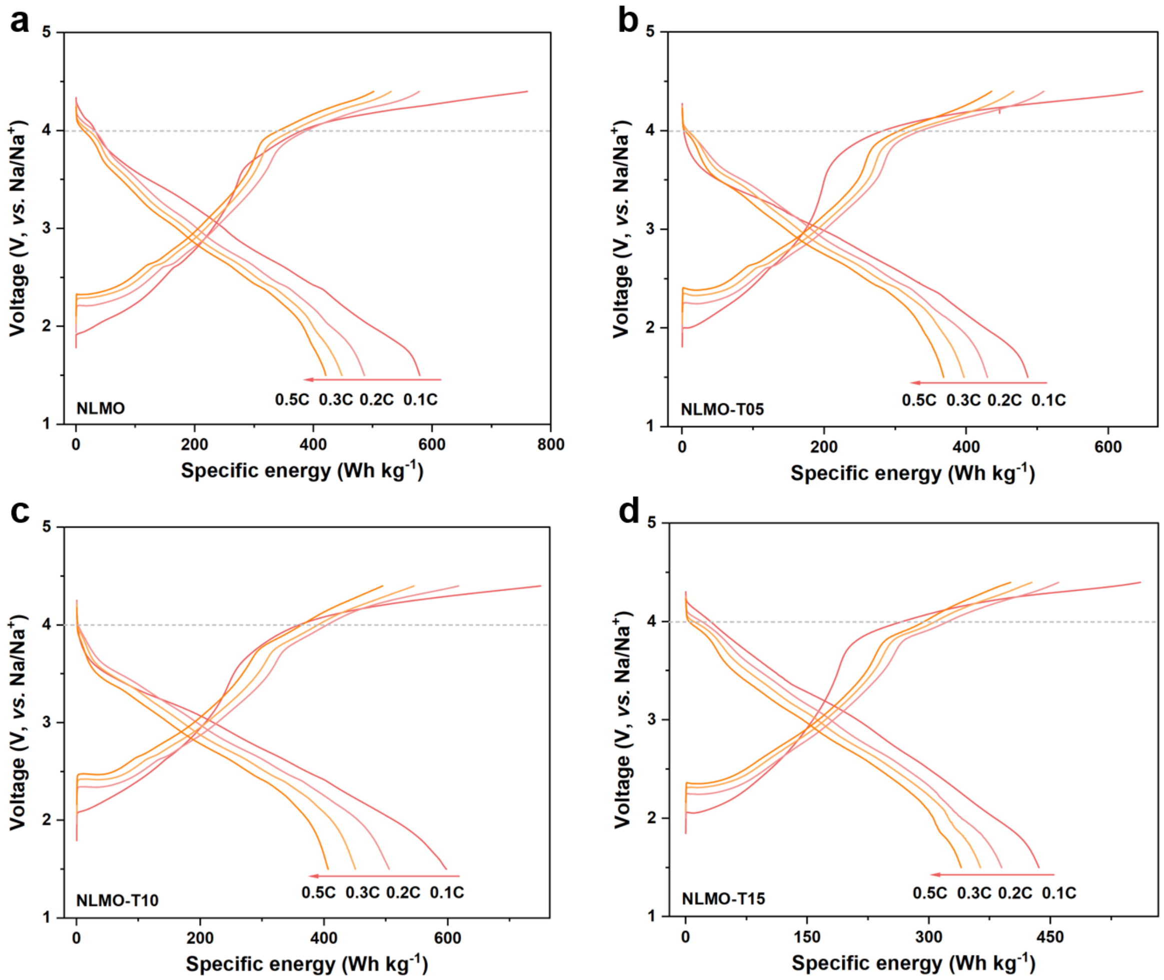

Figure S25. GCD curves versus specific energy of a) NLMO, b) NLMO-T05, c) NLMO-T10, d) NLMO-T15 electrodes at various rates in the voltage range of 1.5−4.4 V.

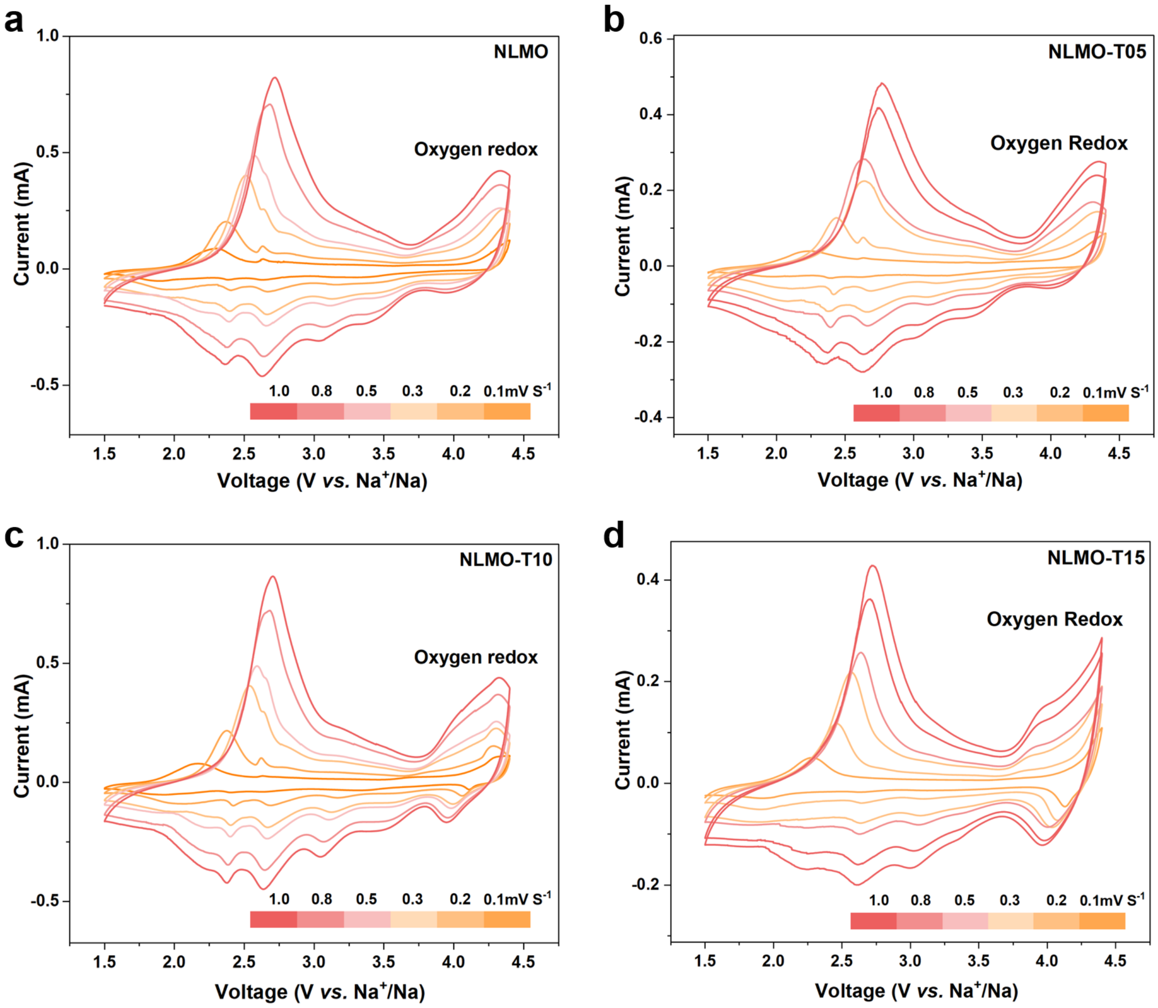

Figure S26. CV curves at different scan rates of a) NLMO, b) NLMO-T05, c) NLMO-T10 and d) NLMO-T15.

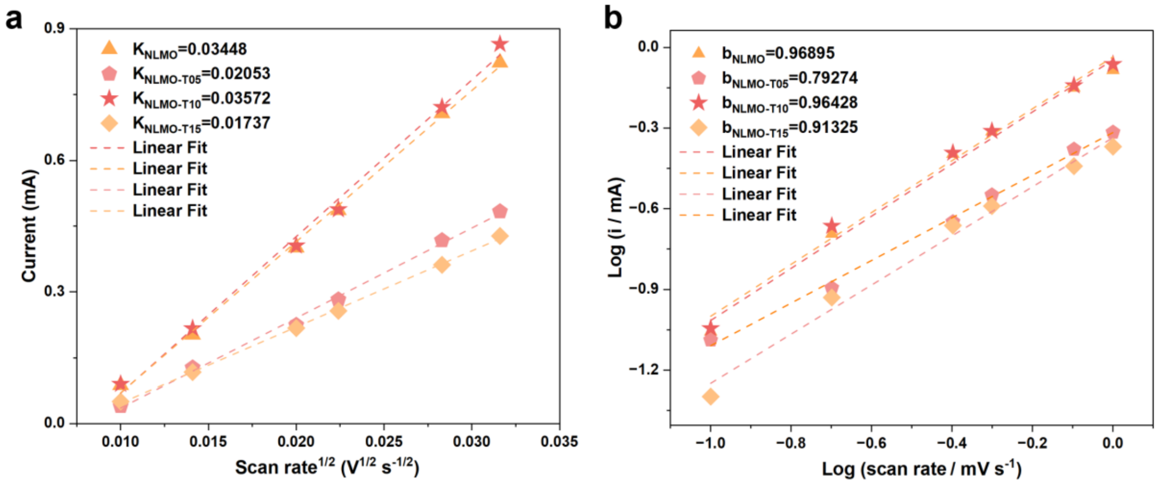

Figure S27. a) Linear fitting of peak current versus square root of the scan rate, b) Linear fitting of log (*i*) versus log (*v*) plots at oxidation peaks.

The Na^+ apparent diffusion coefficient of NLMO-TX electrodes was calculated according to the Randles-Sevcik Equation:

$$I_p=0.4463n^{2/3}F^{3/2}CSR^{-1/2}T^{-1/2}D_{cv}^{1/2}v^{1/2}$$

Where I_p (A) stands for peak current, n stands for the number of elements, F stands for Faraday constant (96485 C mol^{-1}), C (mol cm^{-3}) stands for the bulk concentration in moles per cubic centimeter, S (cm^2) stands for the area of the electrode, R stands for the gas constant (8.314 J mol^{-1} K^{-1}), T (K) stands for the absolute temperature, D_{cv} (cm^2 s^{-1}) stands for the Na^+ apparent diffusion coefficient, and v (V s^{-1}) stands for potential scan rate in volts per second.

a

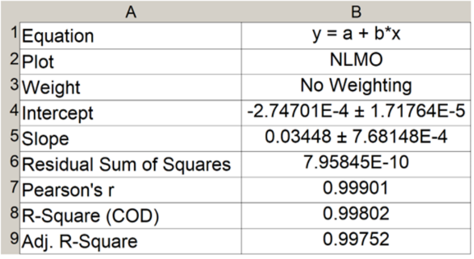

	A	B
1	Equation	y = a + b*x
2	Plot	NLMO
3	Weight	No Weighting
4	Intercept	-2.74701E-4 ± 1.71764E-5
5	Slope	0.03448 ± 7.68148E-4
6	Residual Sum of Squares	7.95845E-10
7	Pearson's r	0.99901
8	R-Square (COD)	0.99802
9	Adj. R-Square	0.99752

b

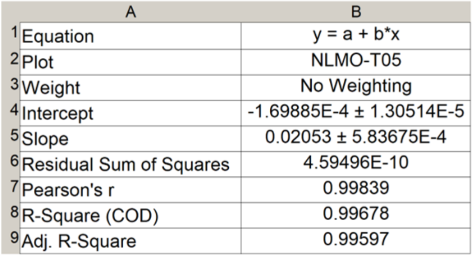

	A	B
1	Equation	y = a + b*x
2	Plot	NLMO-T05
3	Weight	No Weighting
4	Intercept	-1.69885E-4 ± 1.30514E-5
5	Slope	0.02053 ± 5.83675E-4
6	Residual Sum of Squares	4.59496E-10
7	Pearson's r	0.99839
8	R-Square (COD)	0.99678
9	Adj. R-Square	0.99597

c

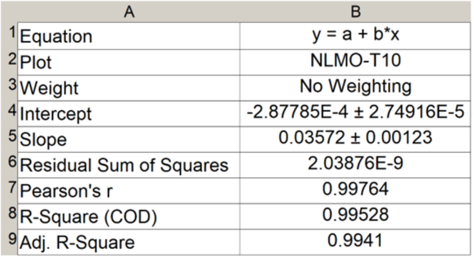

	A	B
1	Equation	y = a + b*x
2	Plot	NLMO-T10
3	Weight	No Weighting
4	Intercept	-2.87785E-4 ± 2.74916E-5
5	Slope	0.03572 ± 0.00123
6	Residual Sum of Squares	2.03876E-9
7	Pearson's r	0.99764
8	R-Square (COD)	0.99528
9	Adj. R-Square	0.9941

d

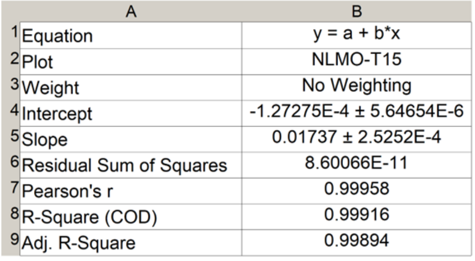

	A	B
1	Equation	y = a + b*x
2	Plot	NLMO-T15
3	Weight	No Weighting
4	Intercept	-1.27275E-4 ± 5.64654E-6
5	Slope	0.01737 ± 2.5252E-4
6	Residual Sum of Squares	8.60066E-11
7	Pearson's r	0.99958
8	R-Square (COD)	0.99916
9	Adj. R-Square	0.99894

e

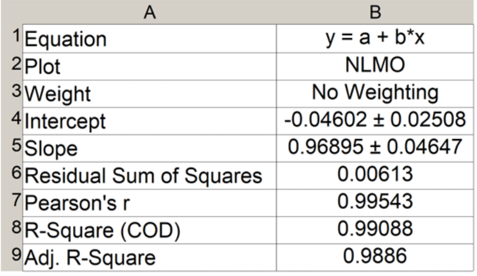

	A	B
1	Equation	y = a + b*x
2	Plot	NLMO
3	Weight	No Weighting
4	Intercept	-0.04602 ± 0.02508
5	Slope	0.96895 ± 0.04647
6	Residual Sum of Squares	0.00613
7	Pearson's r	0.99543
8	R-Square (COD)	0.99088
9	Adj. R-Square	0.9886

f

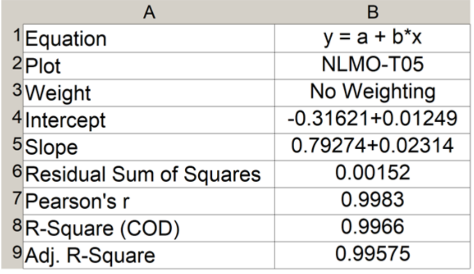

	A	B
1	Equation	y = a + b*x
2	Plot	NLMO-T05
3	Weight	No Weighting
4	Intercept	-0.31621+0.01249
5	Slope	0.79274+0.02314
6	Residual Sum of Squares	0.00152
7	Pearson's r	0.9983
8	R-Square (COD)	0.9966
9	Adj. R-Square	0.99575

g

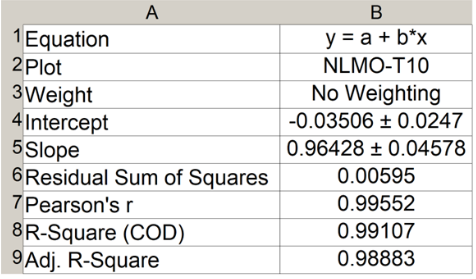

	A	B
1	Equation	y = a + b*x
2	Plot	NLMO-T10
3	Weight	No Weighting
4	Intercept	-0.03506 ± 0.0247
5	Slope	0.96428 ± 0.04578
6	Residual Sum of Squares	0.00595
7	Pearson's r	0.99552
8	R-Square (COD)	0.99107
9	Adj. R-Square	0.98883

h

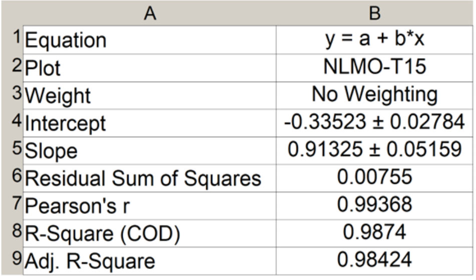

	A	B
1	Equation	y = a + b*x
2	Plot	NLMO-T15
3	Weight	No Weighting
4	Intercept	-0.33523 ± 0.02784
5	Slope	0.91325 ± 0.05159
6	Residual Sum of Squares	0.00755
7	Pearson's r	0.99368
8	R-Square (COD)	0.9874
9	Adj. R-Square	0.98424

Figure S28. The results of linear fitting of peak current versus square root of the scan rate of a) NLMO, b) NLMO-T05, c) NLMO-T10 and d) NLMO-T15 electrodes at oxidation peaks. The results of linear fitting concerning the log (*i*) versus log (*v*) plots of e) NLMO, f) NLMO-T05, g) NLMO-T10 and h) NLMO-T15 electrode at oxidation peaks.

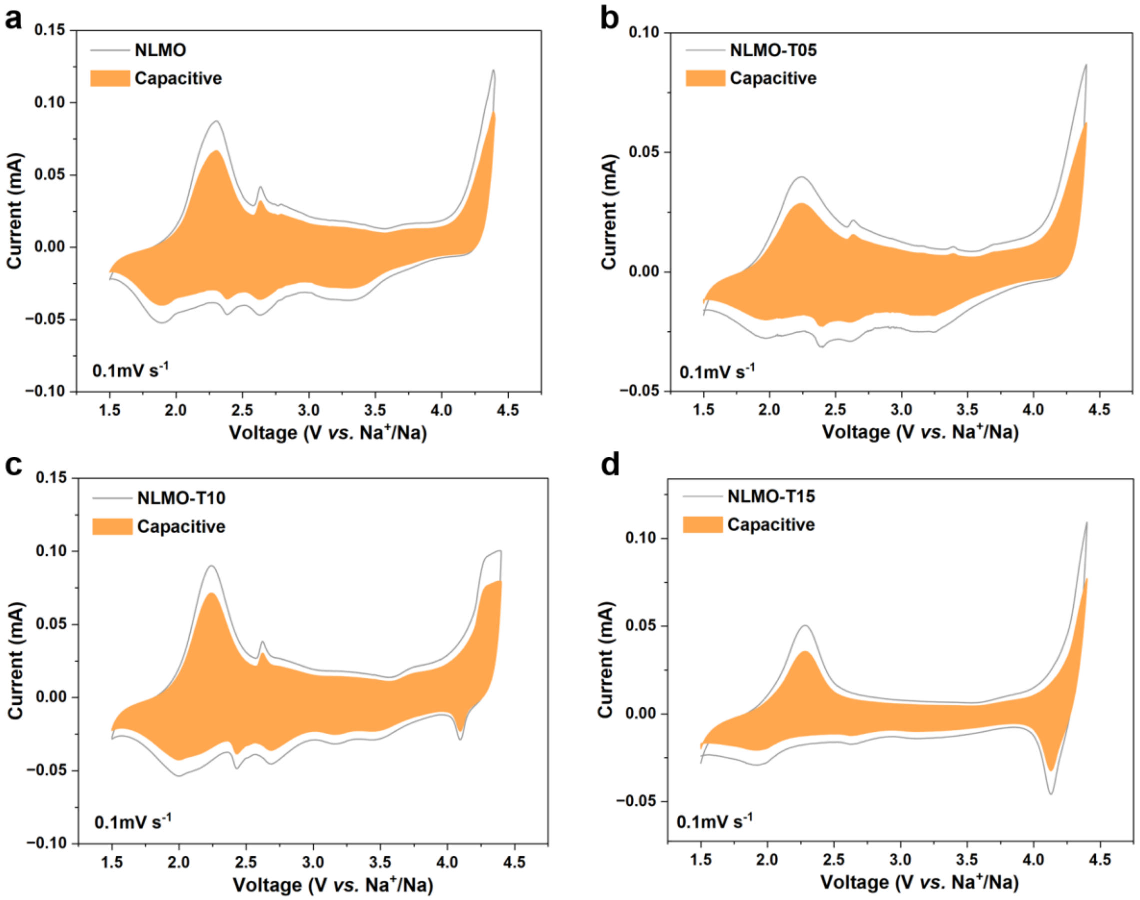

Figure S29. The Fitted pseudo-capacitive contribution (orange area) of a) NLMO, b) NLMO-T05, c) NLMO-T10 and d) NLMO-T15 electrodes at 0.1 mV s^{-1}.

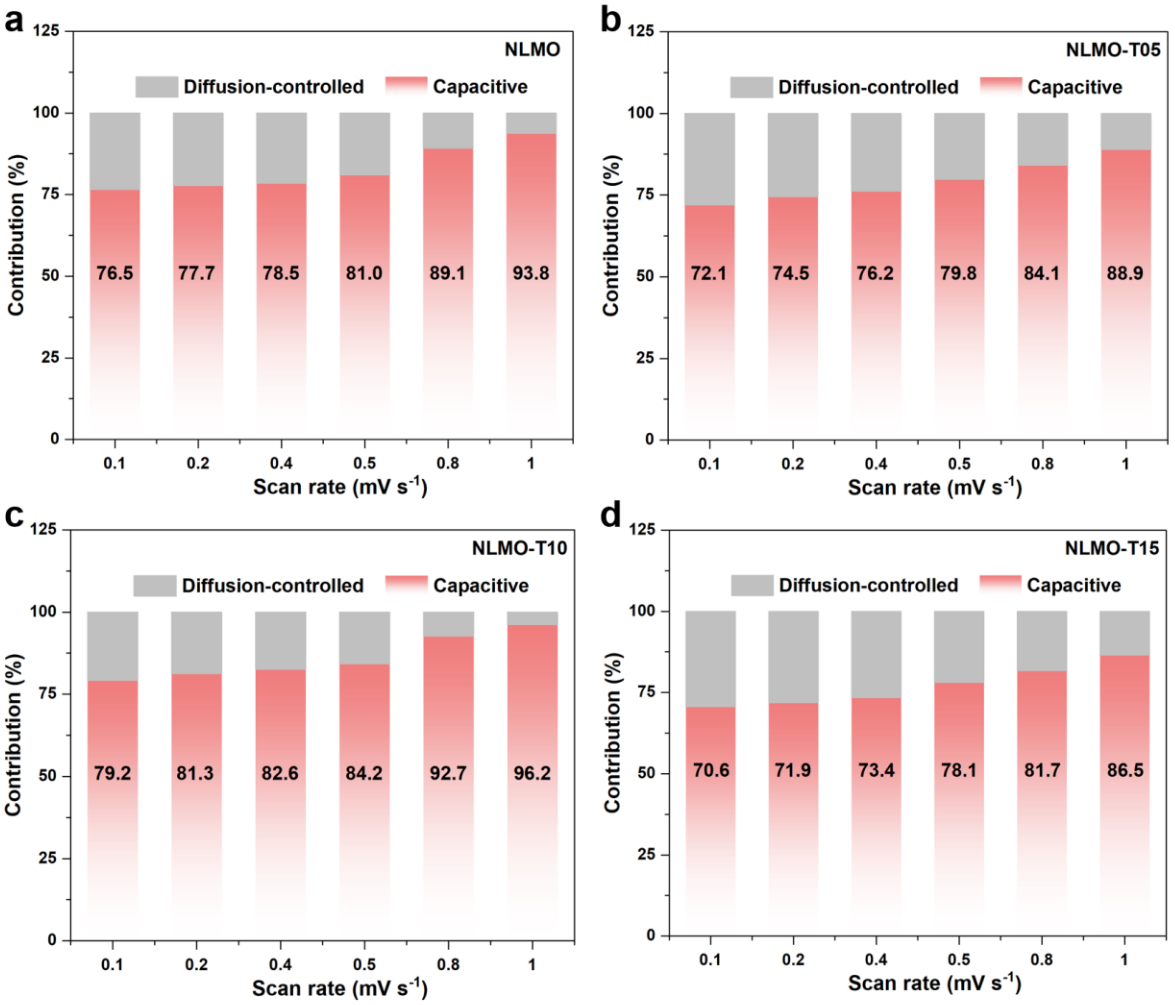

Figure S30. The ratio of the pseudo-capacitive and diffusion-controlled capacities of a) NLMO, b) NLMO-T05, c) NLMO-T10 and d) NLMO-T15 electrodes at different scan rates.

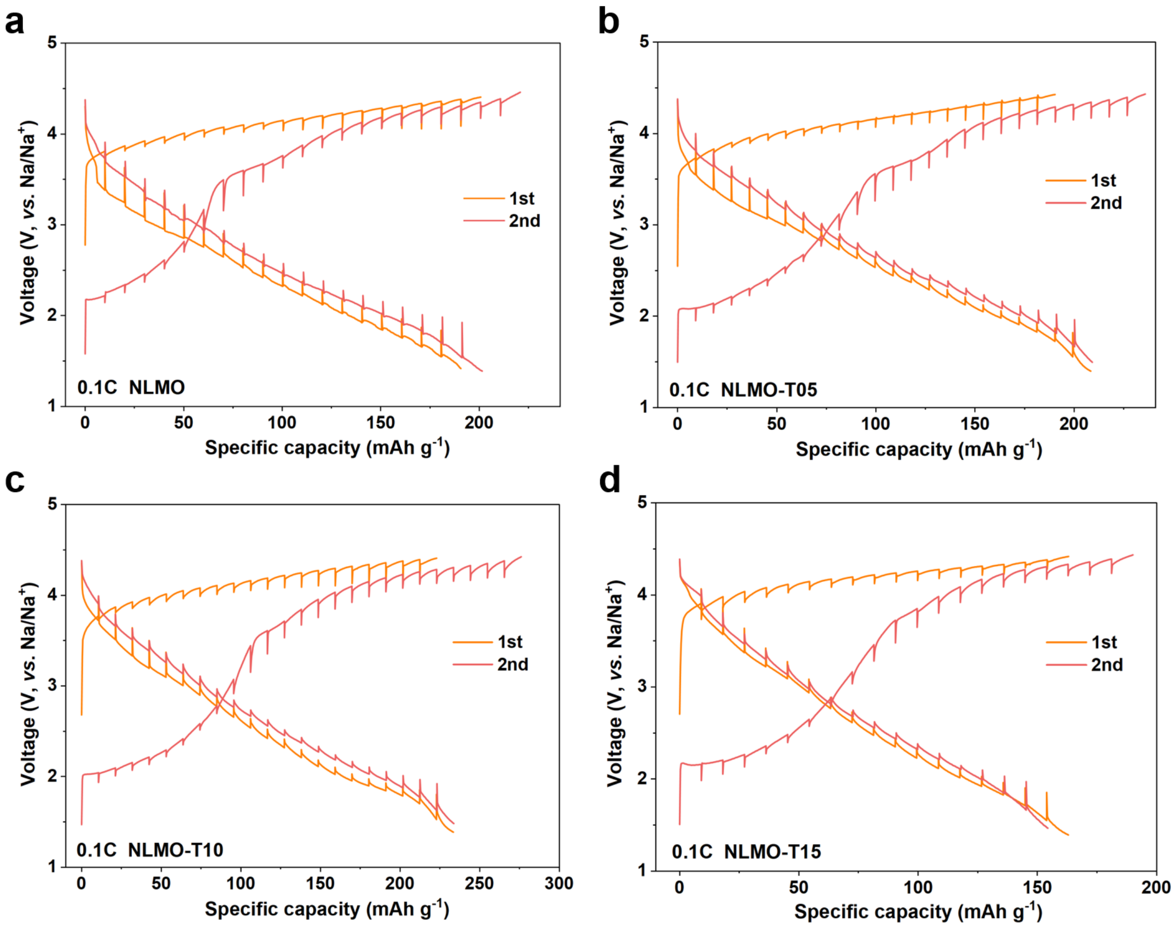

Figure S31. GITT curves at 0.1 C of a) NLMO, b) NLMO-T05, c) NLMO-T10 and d) NLMO-T15 electrodes in the voltage range of 1.5−4.4 V.

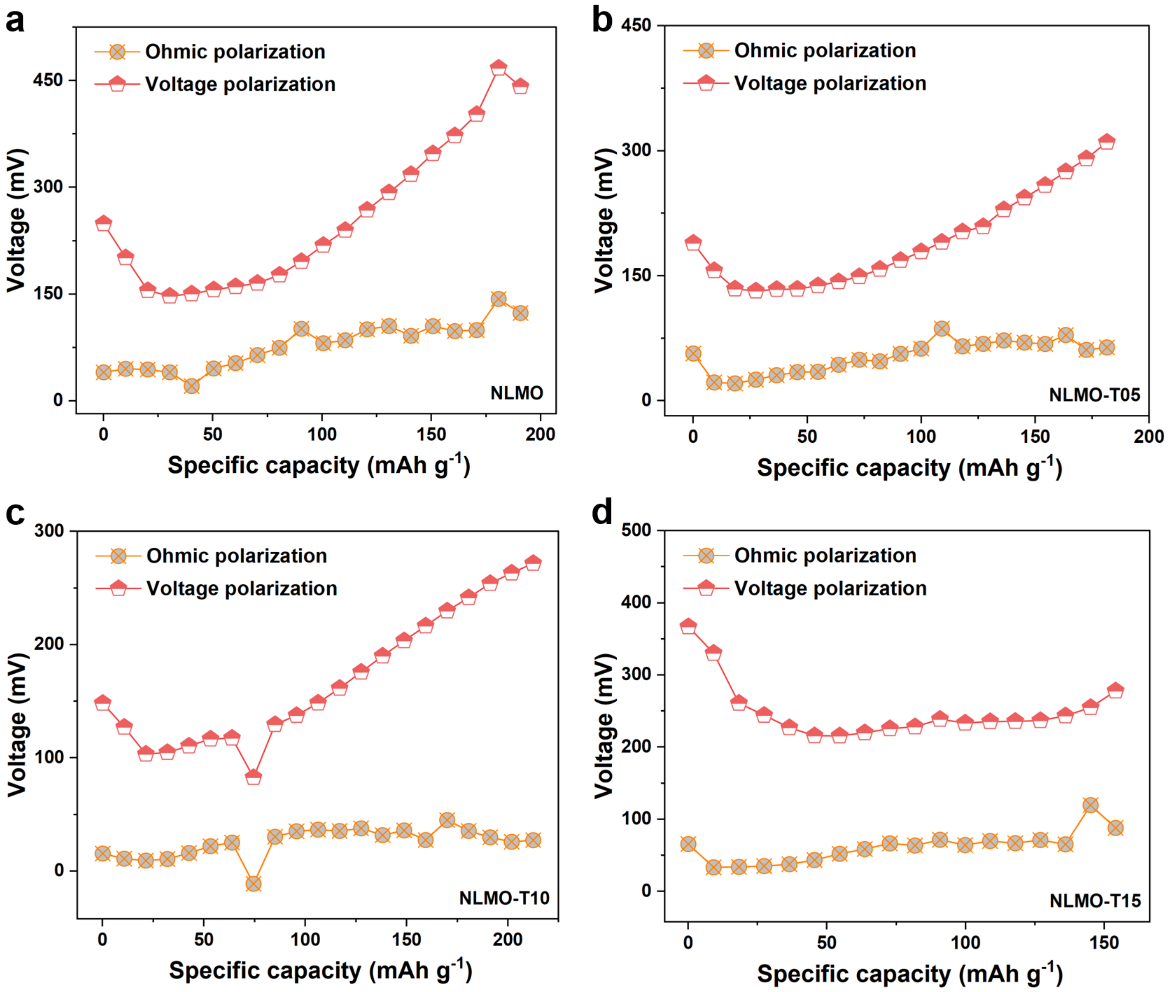

Figure S32. Ohmic polarization and voltage polarization and of a) NLMO, b) NLMO-T05, c) NLMO-T10 and d) NLMO-T15 electrodes in the initial charging process.

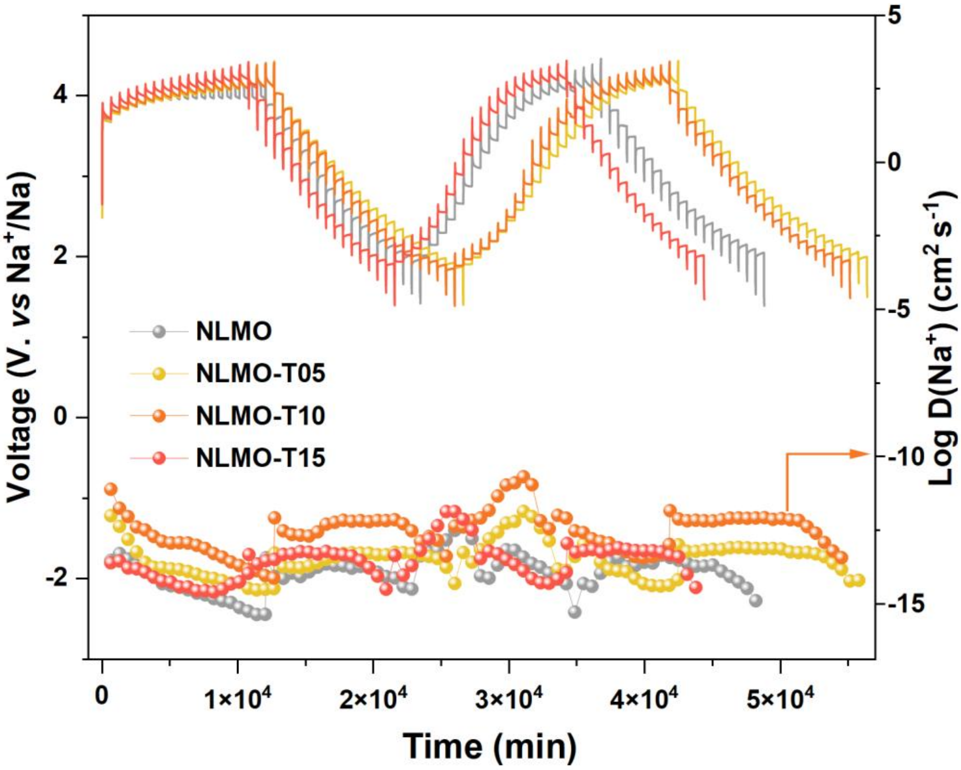

Figure S33. GITT curves and Na^+ diffusion coefficients of NLMO-TX electrodes.

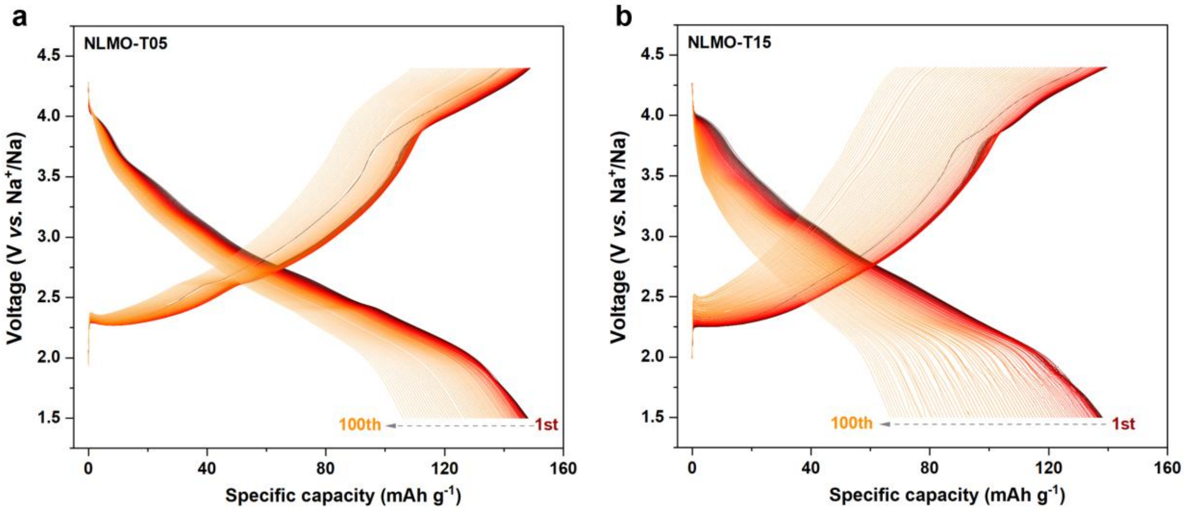

Figure S34. GCD curves of a) NLMO-05 and b) NLMO-T15 electrodes during cycling process.

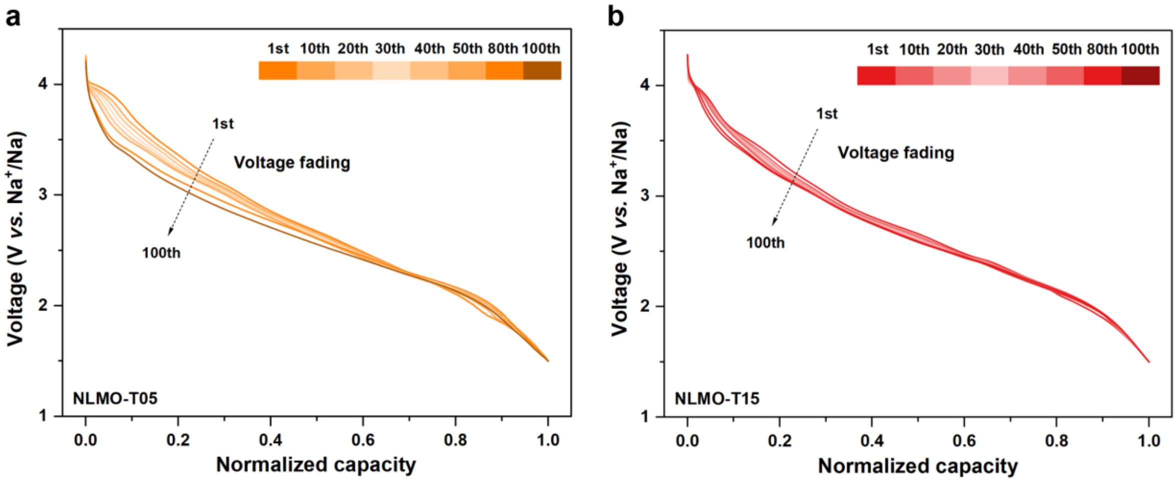

Figure S35. Normalized discharge curves of a) NLMO-05 and b) NLMO-T15 electrodes during cycling process.

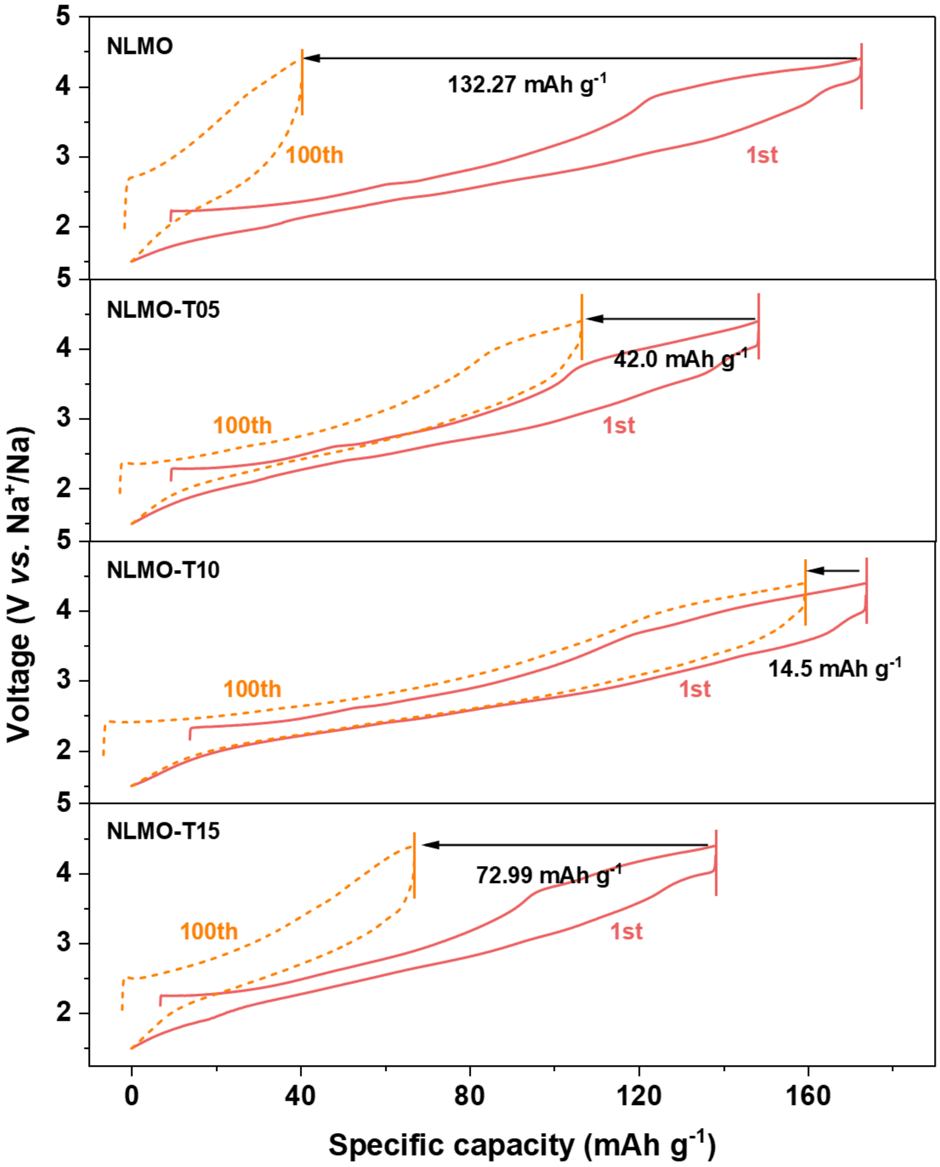

Figure S36. GCD curves versus specific capacity in 1st and 100th cycles at 0.2 C of NLMO, NLMO-T05, NLMO-T10 and NLMO-T15 electrodes.

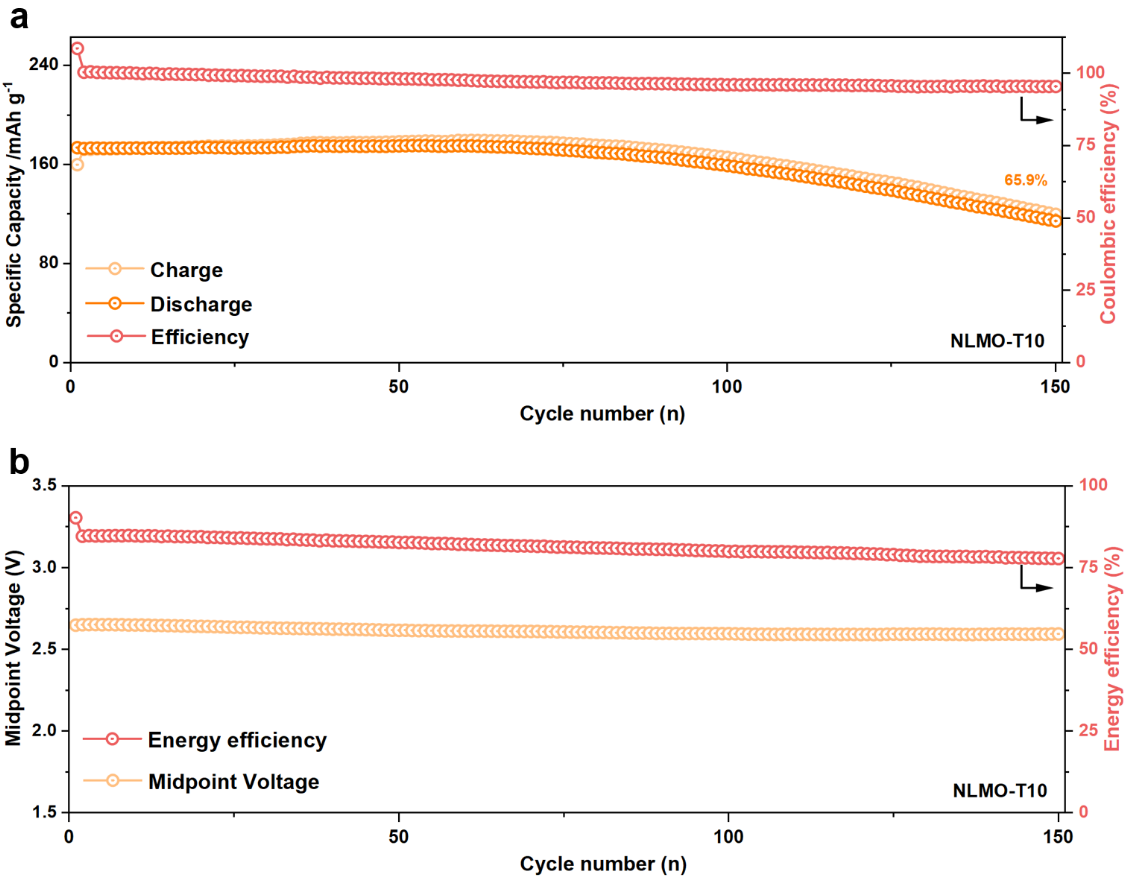

Figure S37. a) Cycling performance of NLMO-T10 over 150 cycles at 0.2 C after rate performance tests. b) Energy efficiency and midpoint voltage during 150 cycles at 0.5 C of NLMO-T10 electrode in the voltage range of 1.5−4.4 V.

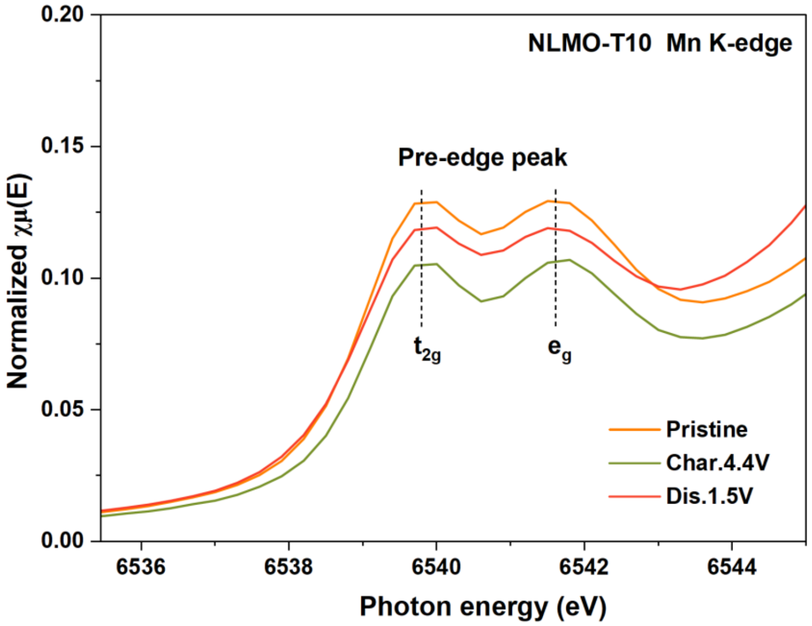

Figure S38. *Ex-situ* XAS spectra of Mn *K*-edge for NLMO-T10 at pre-edge peak.

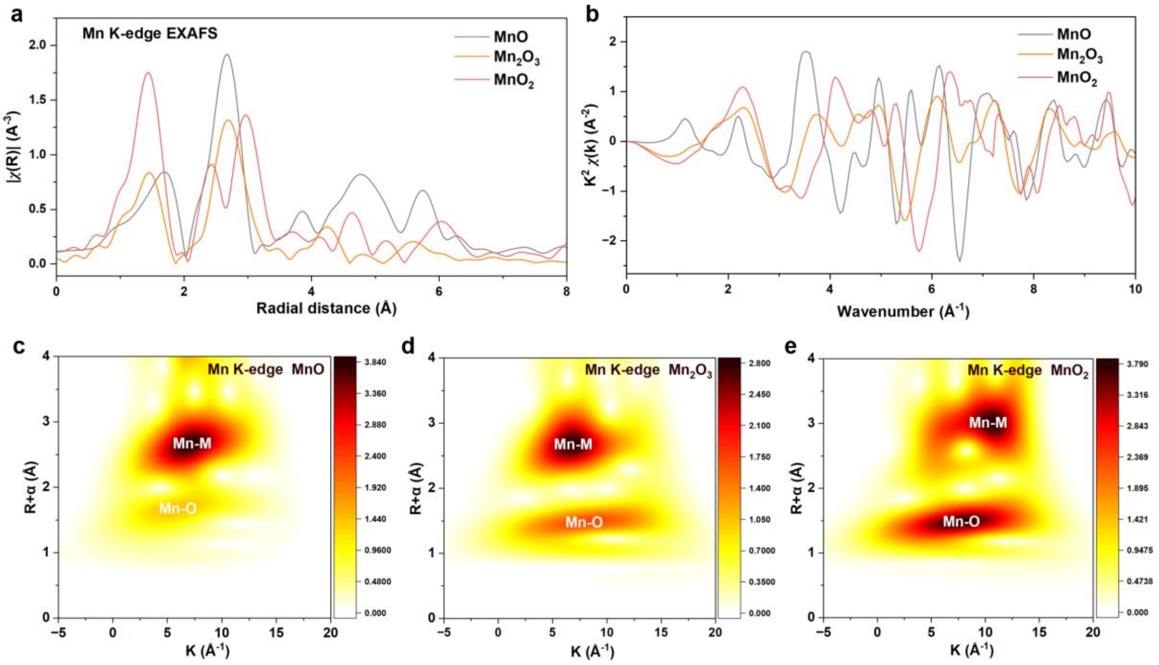

Figure S39. EXAFS a) R space and b) K space curves of Mn *K*-edge for MnO, Mn_2O_3 and MnO_2. WT-EXAFS spectra of Mn *K*-edge for c) MnO (Mn^{2+}), d) Mn_2O_3 (Mn^{3+}) and e) MnO_2 (Mn^{4+}).

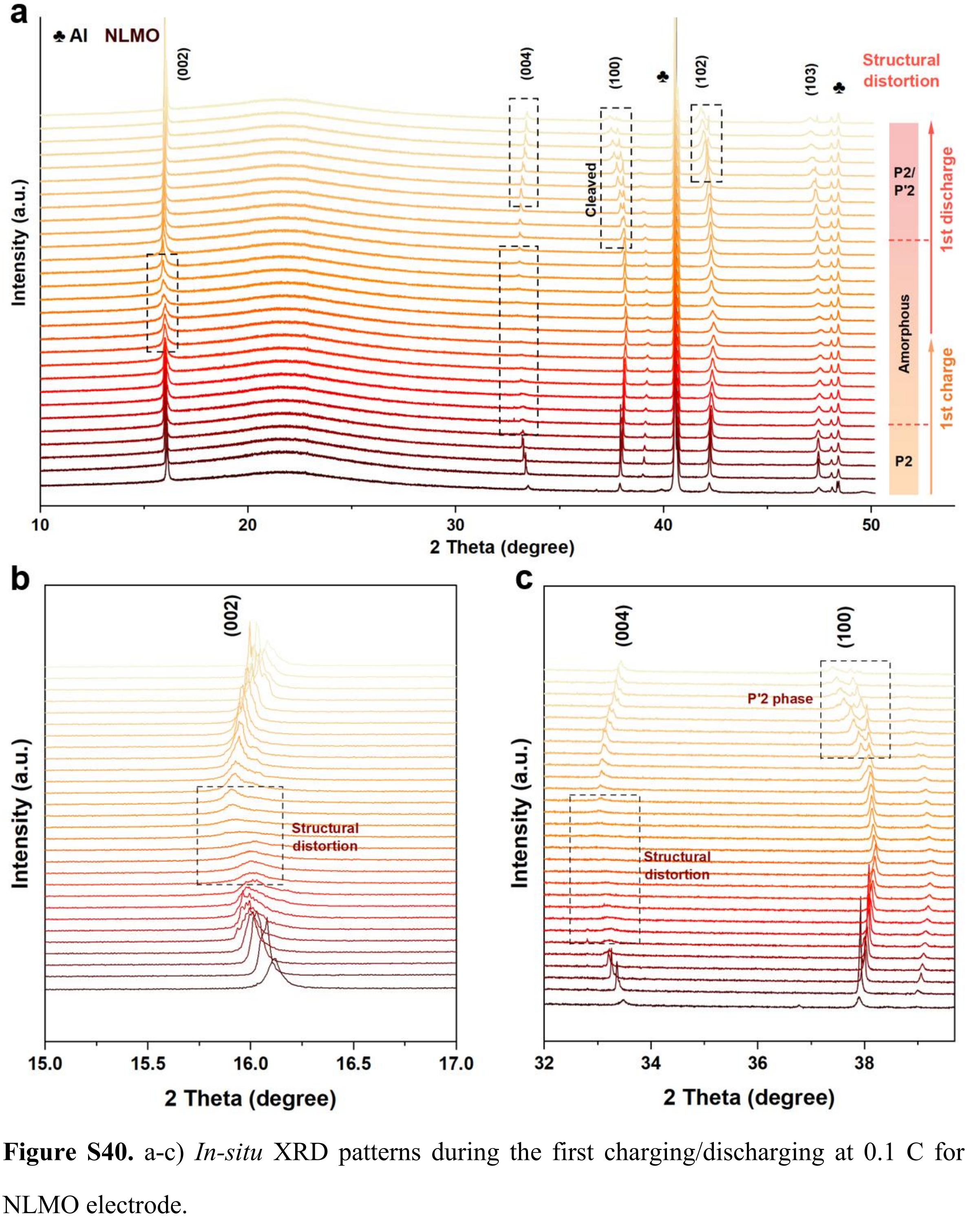

Figure S40. a-c) *In-situ* XRD patterns during the first charging/discharging at 0.1 C for NLMO electrode.

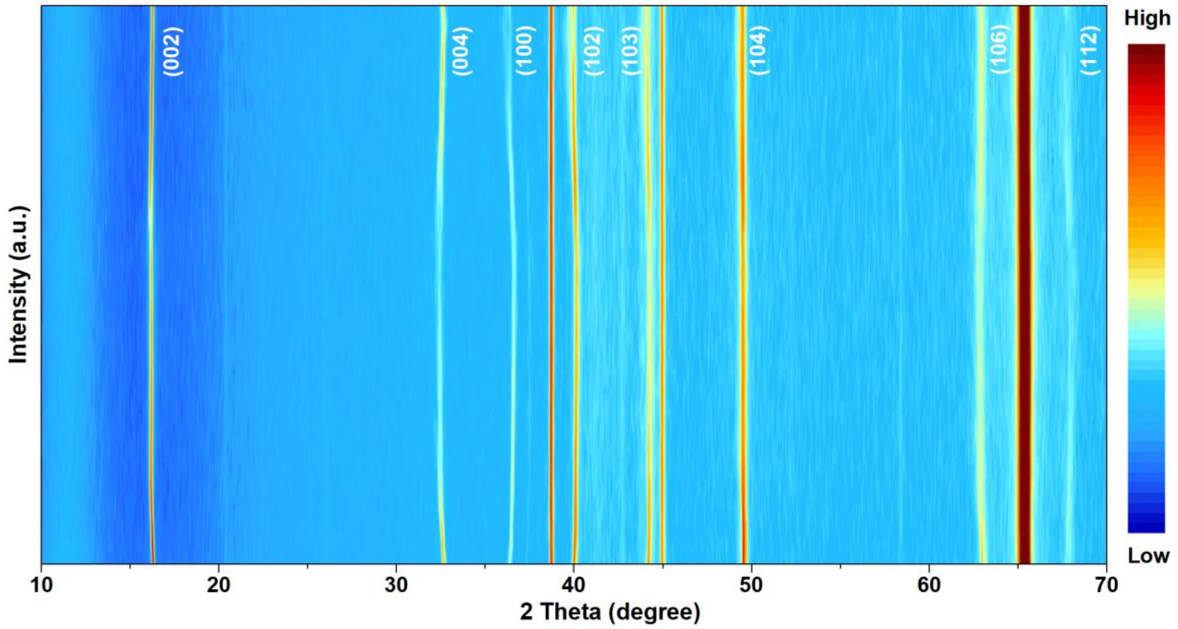

Figure S41. Intensity contour maps (bird's eye view) of *in-situ* XRD patterns of NLMO-T10 cathode materials during the first charge/discharge at 0.1 C.

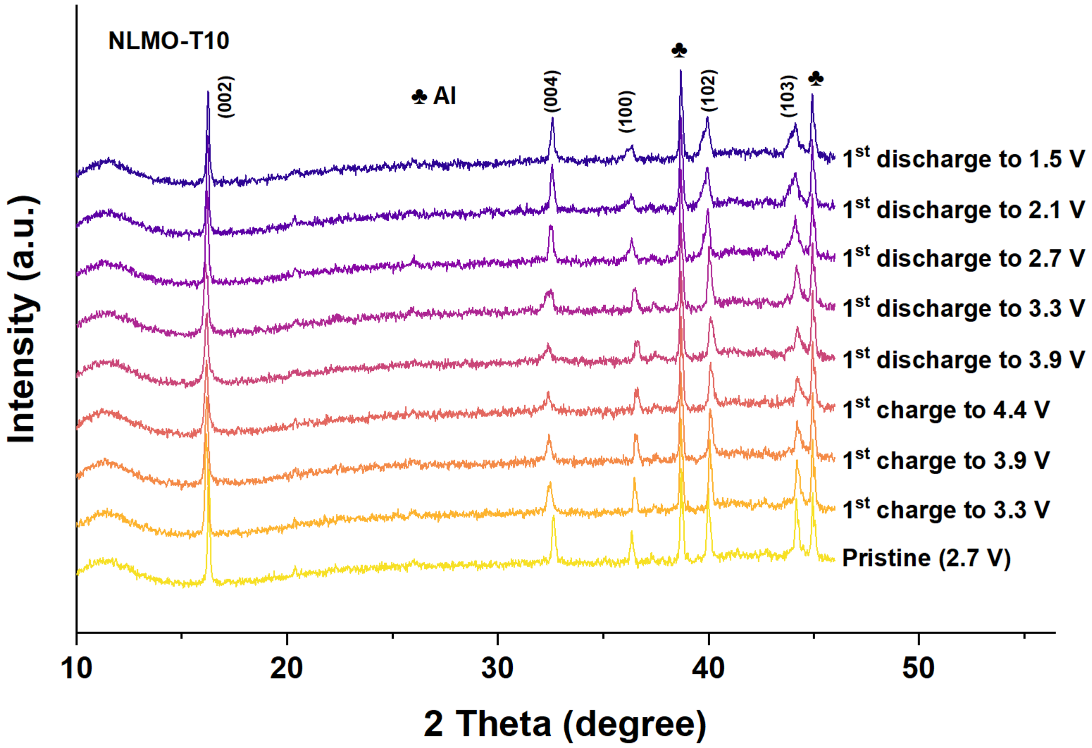

Figure S42. Detailed *in-situ* XRD patterns of NLMO-T10 cathode materials at different charge and discharge voltages.

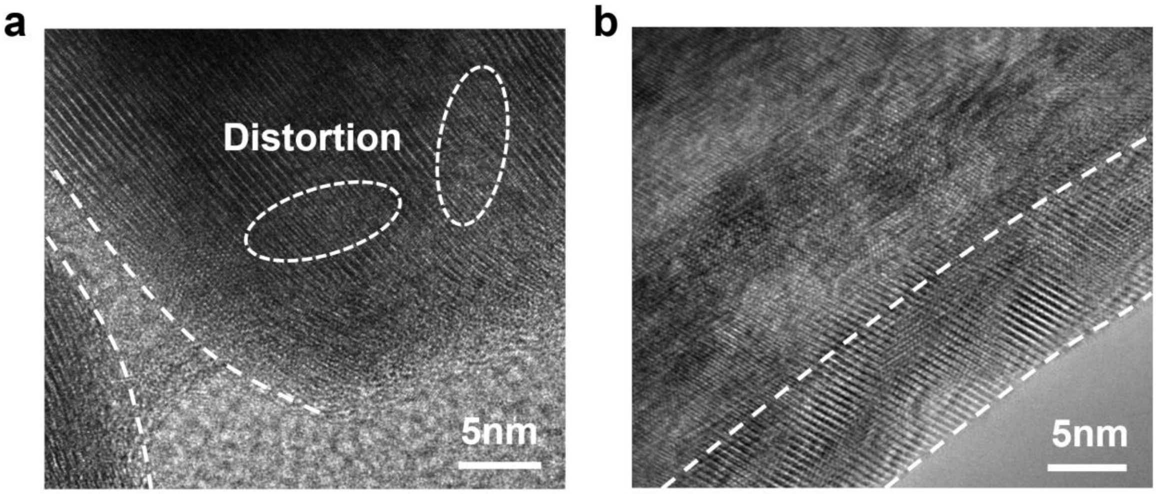

Figure S43. HRTEM images of a) NLMO and b) NLMO-T10 cathode materials after cycles.

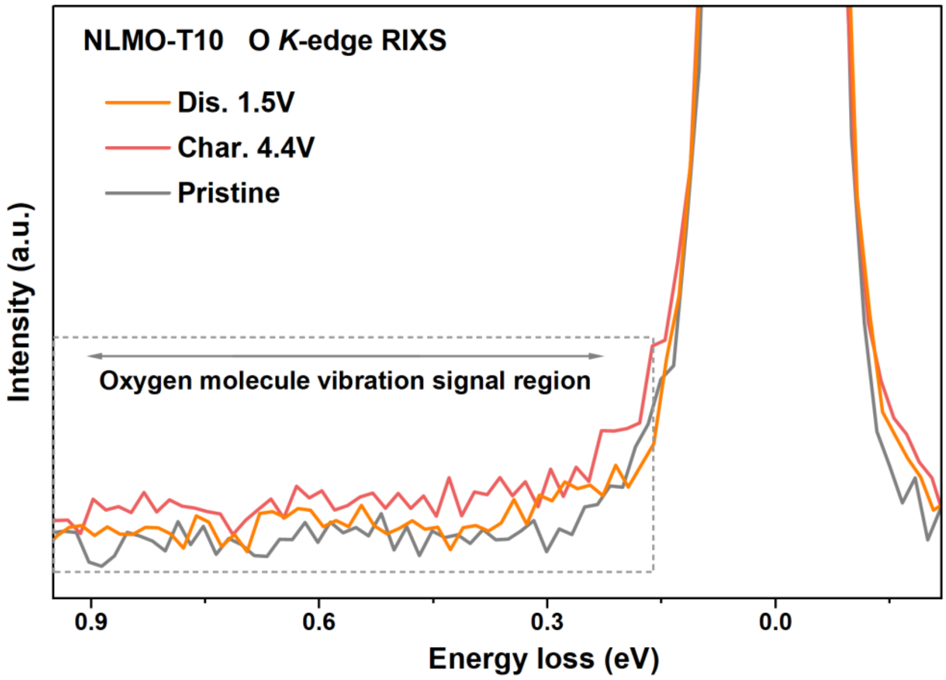

Figure S44. O *K*-edge RIXS spectra with an excitation energy of 531 eV for NLMO-T10 in different charge and discharge states at the region of loss energy close to 0 eV.

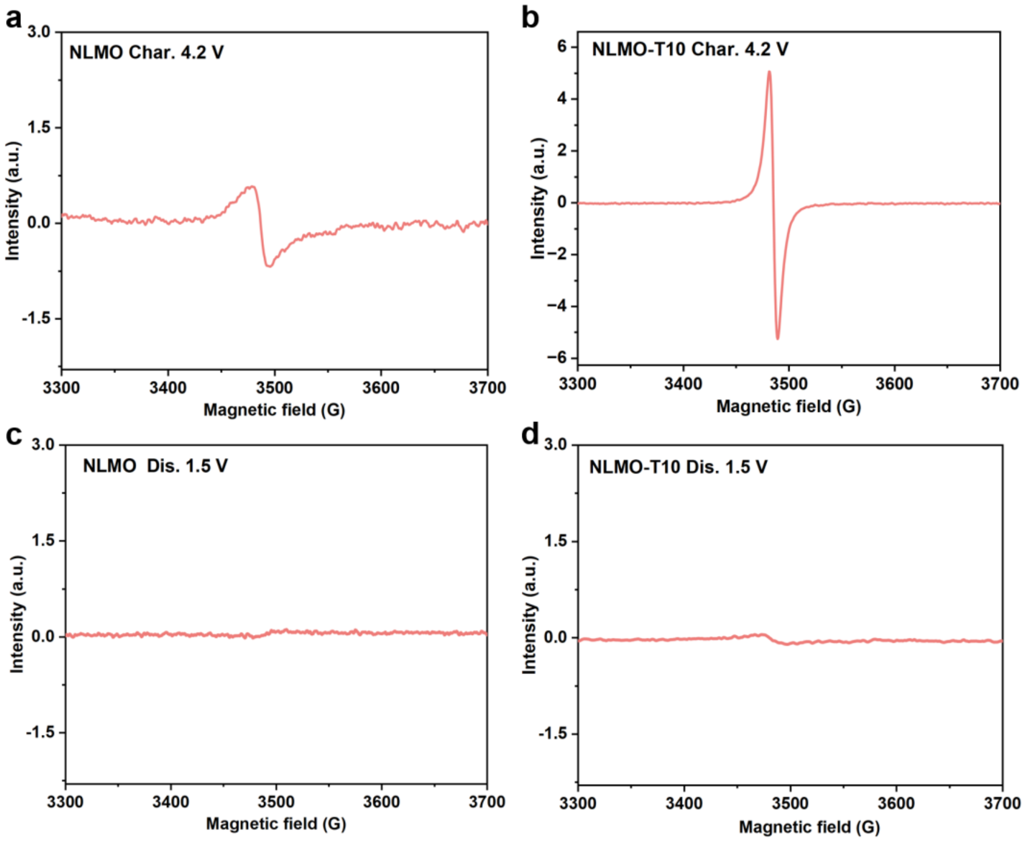

Figure S45. *Ex-situ* EPR spectra of a) NLMO and b) NLMO-T10 when charged to 4.2 V, *Ex-situ* EPR spectra of c) NLMO and d) NLMO-T10 when discharged to 1.5 V.

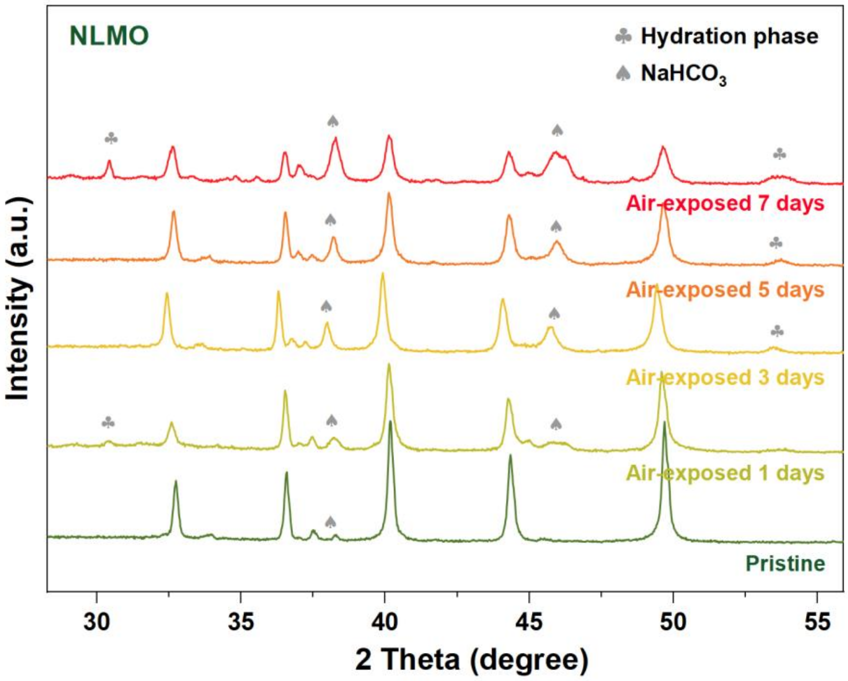

Figure S46. Enlarged XRD patterns of NLMO samples exposed to air for different days.

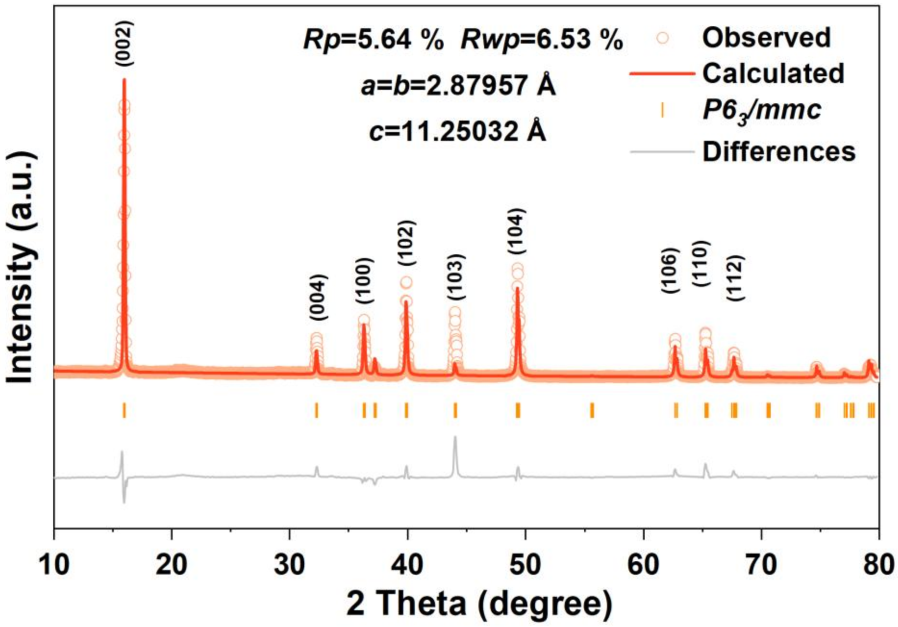

Figure S47. XRD Rietveld refinement results for NLMO-T10 samples exposed to air for 7 days.

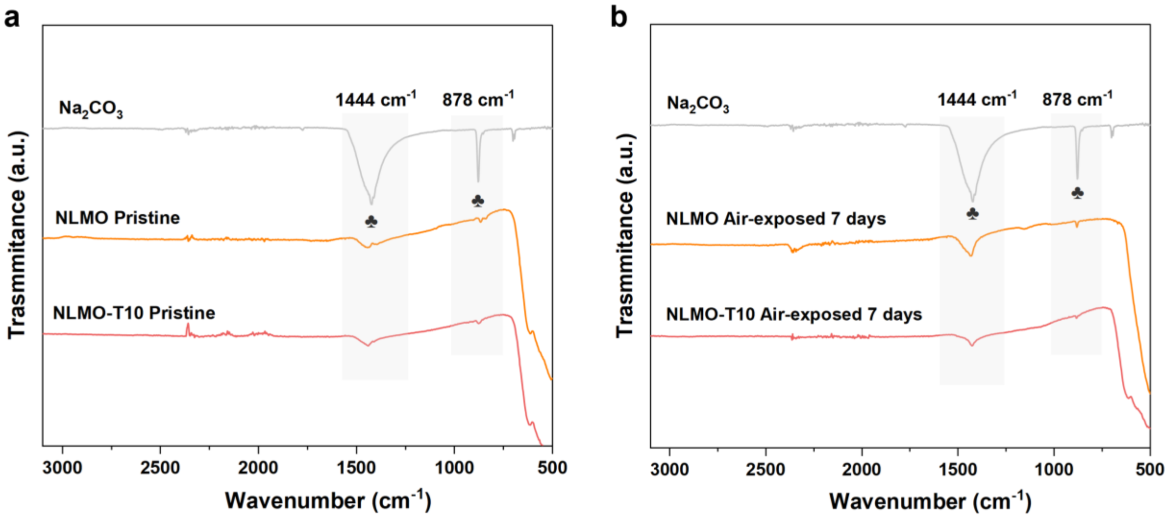

Figure S48. a) FTIR patterns of Na_2CO_3, NLMO pristine samples and NLMO-T10 pristine samples. b) FTIR patterns of Na_2CO_3, air-exposed NLMO samples and air-exposed NLMO-T10 samples.

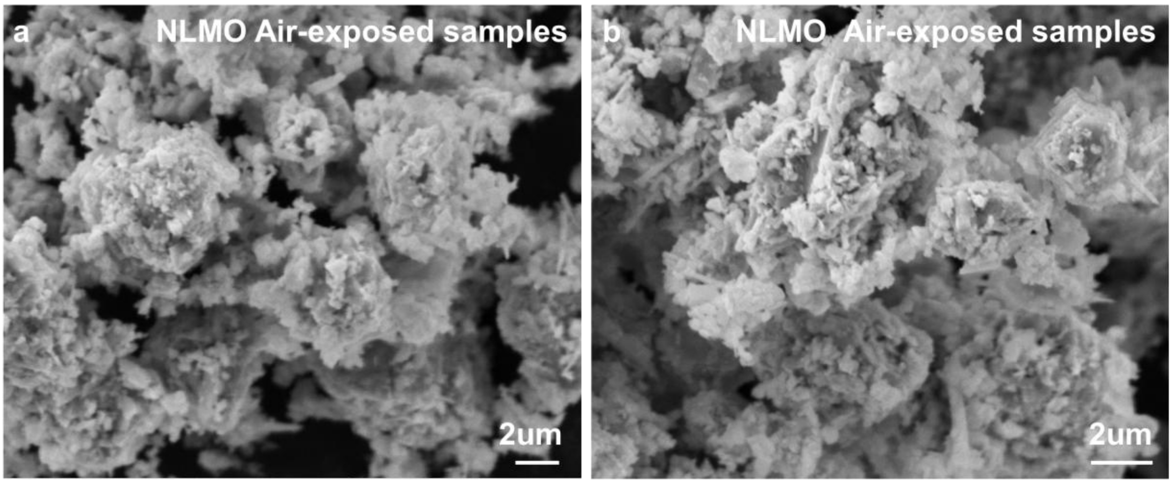

Figure S49. a, b) SEM images of air-exposed NLMO samples.

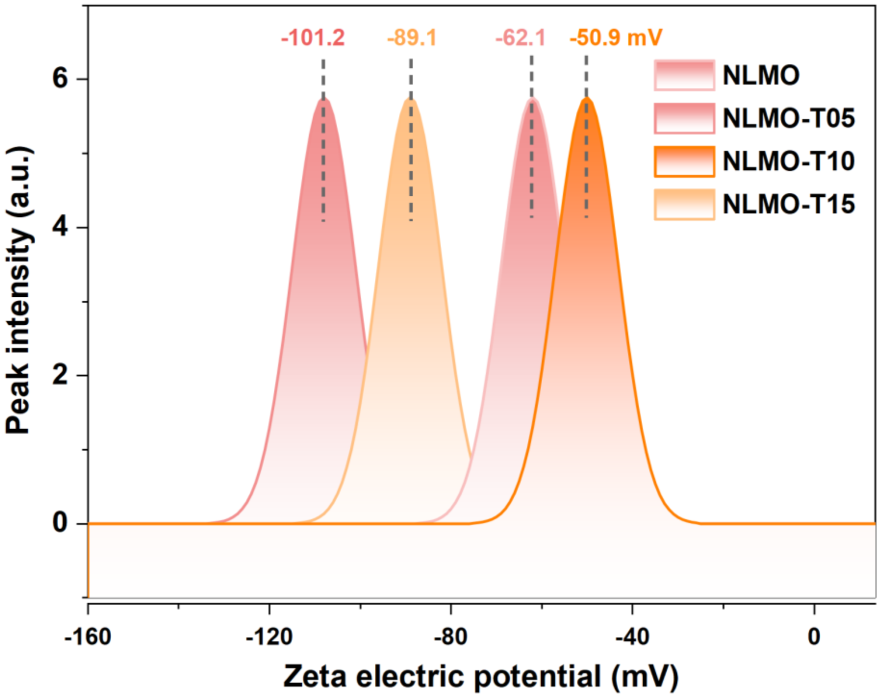

Figure S50. Zeta electric potential results of NLMO, NLMO-T05, NLMO-T10 and NLMO-T15 cathode materials.

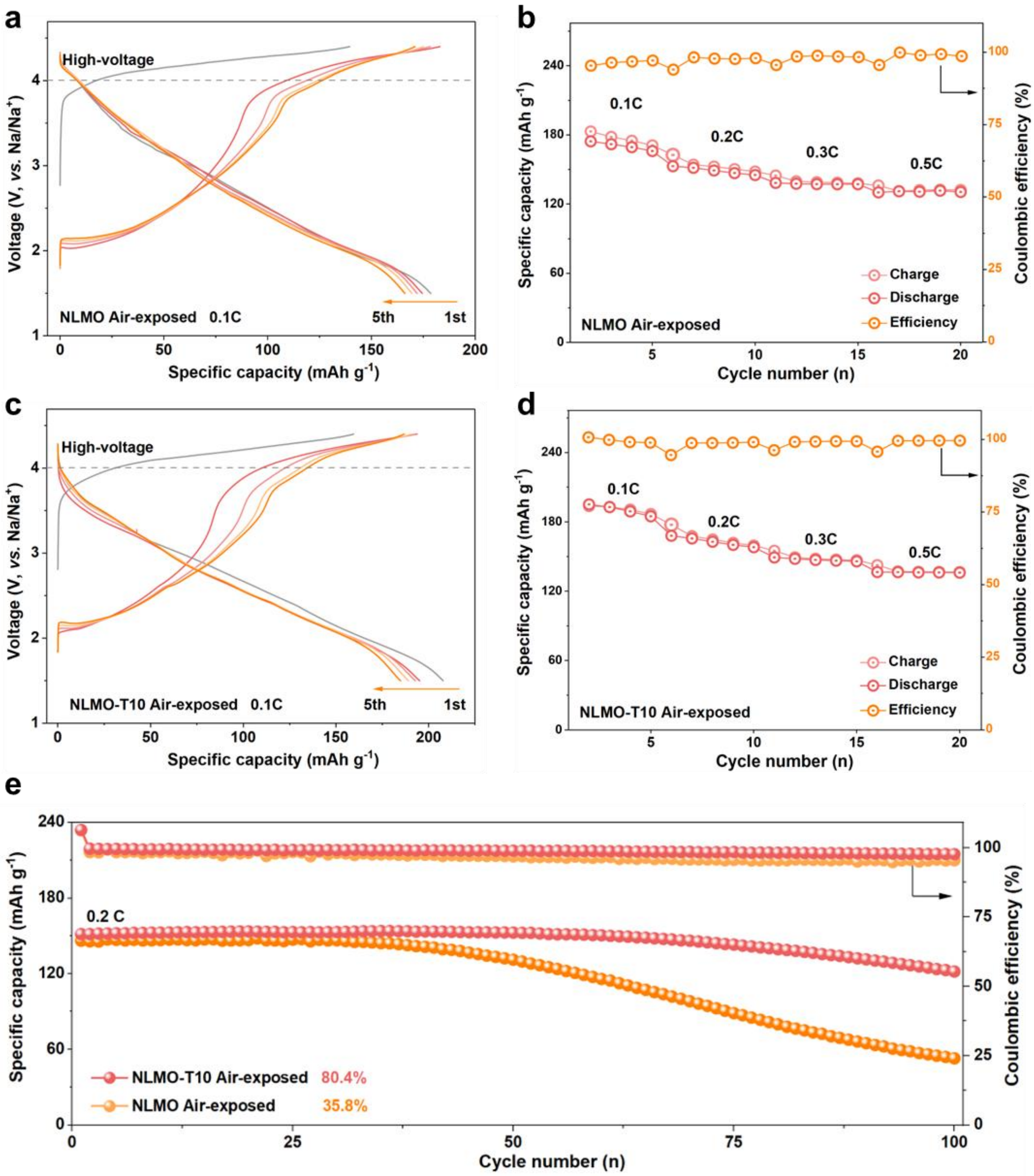

Figure S51. a, c) GCD curves versus specific capacity of air-exposed NLMO and NLMO-T10 electrodes at 0.1 C in the voltage range of 1.5−4.4 V. b, d) Rate performance of air-exposed NLMO and NLMO-T10 electrodes at various rates in the voltage range of 1.5−4.4 V. e) Cycling performance of air-exposed NLMO and NLMO-T10 sample during 100 cycles at 0.2 C after rate performance tests.

Table S1. Crystallographic parameters of NLMO, NLMO-T10 and air-exposed NLMO-T10 cathode materials refined by the Rietveld method.

Sample	**NLMO**	**NLMO-T10**	**Air exposed-NLMO-T10**
Space group	$P6_3/mmc$	$P6_3/mmc$	$P6_3/mmc$
a **(Å)**	2.88536	2.88673	2.87957
b **(Å)**	2.88536	2.88673	2.87957
c **(Å)**	11.22388	11.23648	11.25032
χ^2	8.24	4.22	6.57
R_p **(%)**	2.49	3.59	5.64
R_{wp} **(%)**	4.04	4.23	6.53

Table S2. Specific parameters of electrochemical performance of NLMO electrode in the voltage range of 1.5−4.4 V.

NLMO	0.1C	0.2C	0.3C	0.5C
Time	12h 50min	5h 24min	3h 06min	1h 49min
Specific Capacity (mAh g^{-1})	230.42/ 216.03	194.98/ 183.13	167.69/ 165.55	164.33/ 156.73
Energy Density (Wh Kg^{-1})	701.72/ 567.64	577.88/ 485.48	530.43/ 477.51	501.16/ 420.50

Table S3. Specific parameters of electrochemical performance of NLMO-T10 electrode in the voltage range of 1.5−4.4 V.

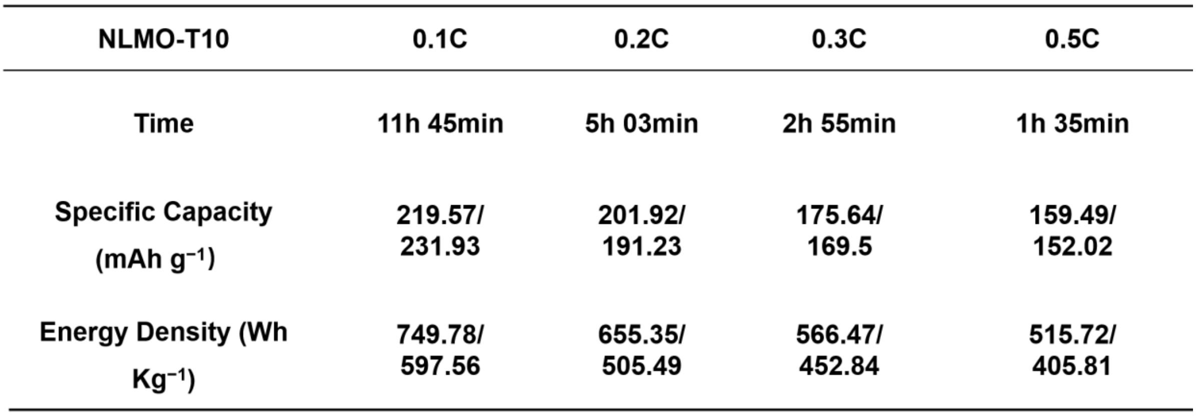

NLMO-T10	0.1C	0.2C	0.3C	0.5C
Time	11h 45min	5h 03min	2h 55min	1h 35min
Specific Capacity (mAh g^{-1})	219.57/ 231.93	201.92/ 191.23	175.64/ 169.5	159.49/ 152.02
Energy Density (Wh Kg^{-1})	749.78/ 597.56	655.35/ 505.49	566.47/ 452.84	515.72/ 405.81

Table S4. Na^+ Diffusion coefficients of NLMO, NLMO-T05, NLMO-T10 and NLMO-T15 electrodes calculated by fitting and combining CV curves at different sweep speeds.

Sample	**Diffusion coefficient (D Na^+)**
NLMO	6.876×10^{-12} cm^2 s^{-1}
NLMO-T05	2.438×10^{-12} cm^2 s^{-1}
NLMO-T10	7.380×10^{-11} cm^2 s^{-1}
NLMO-T15	1.746×10^{-12} cm^2 s^{-1}

Table S5. Comprehensive comparison of the electrochemical performance parameters of NLMO-T10 with previously reported cathode materials.[1-35]

Type	Cathode material	Voltage range (V)	Specific capacity (mAh g^{-1})	Energy density (Wh Kg^{-1})	Average voltage (V)	Ref.
Polyanionic Compounds	$Na_2Fe_2(SO_4)_3$	2.0-4.5	100.5	366.2	3.68	1
	$Na_4Co_3(PO_4)_2P_2O_7$	3.0-4.7	95.2	425.6	4.4	2
	Na_2CoPO_4F	3.0-4.7	102.3	418.7	4.3	3
	$Na_3(VOPO_4)_2F$	2.5-4.5	115.2	408.1	3.6	4
	$Na_3V_2(PO_4)_2F_3$	2.5-4.5	121.6	431.6	3.62	5
	$Na_2MnP_2O_7$	2.0-4.5	76.5	268.2	3.48	6
	$Na_3V_2(PO_4)_3$	2.7-3.8	120.7	434.7	3.34	7
	Na_2FePO_4F	2.0-4.0	103.5	289.3	2.785	8
	$NaFe(SO_4)_2$	2.0-4.2	89.5	248.2	2.77	9
	$NaFePO_4$	1.5-4.2	150.7	392.7	2.58	10
Prussian Blue Analogs	$Na_4Fe(CN)_6$	1.5-3.9	102.3	328.4	3.25	11
	$Na_{1.72}Mn[Fe(CN)_6]$	2.0-4.2	133.4	398.3	3	12
	$Na_{1.92}Mn[Fe(CN)_6]$	2.0-4.0	158.3	488.2	3.1	13
	$Na_2Mn[Mn(CN)_6]$	2.0-4.2	206.3	503.1	2.45	14
Transition Metal Oxides	$Na_{7/9}Cu_{2/9}Fe_{1/9}Mn_{2/3}O_2$	2.5-4.2	92.5	349.4	3.7	15
	$NaNi_{1/2}Ti_{1/2}O_2$	2.0-4.2	101.4	312.5	3.12	16
	$NaNi_{2/3}Sb_{1/3}O_2$	2.5-4.0	115.4	338.2	3	17
	$Na_{0.44}MnO_2$	2.0-4.0	100.6	287.4	2.67	18
	$Na_{0.44}Mn_{0.85}Ti_{0.15}O_2$	2.0-4.0	105.3	284.2	2.49	19
	$NaNi_{1/3}Fe_{1/3}Mn_{1/3}O_2$	2.0-4.0	131.4	394.3	2.98	20
	$Na_{0.7}MnO_2$	2.0-3.8	162.4	448.8	2.77	21
	$NaNi_{1/2}Mn_{1/2}O_2$	1.5-4.3	141.2	558.2	2.9	22
	$Na_{2/3}Fe_{1/2}Mn_{1/2}O_2$	1.5-4.3	187.5	513.4	2.75	23
	$Na_{2/3}Mn_{8/9}Ti_{1/9}O_2$	1.5-4.3	193.8	536.0	2.77	24
	$Na_{2/3}Mg_{0.28}Mn_{0.72}O_2$	1.5-4.5	221.3	574.3	2.58	25
	$Na_{2/3}Mn_{0.8}Fe_{0.1}Ti_{0.1}O_2$	2.0-4.0	144.7	428.7	3	26
	$Na_{5/6}Li_{1/4}Mn_{3/4}O_2$	1.5-4.5	200.3	501.5	2.5	27
	$Na_{2/3}Ni_{1/3}Mn_{1/3}Ti_{1/6}O_2$	2.5-4.35	126.4	469.7	3.73	28
	$NaNi_{0.4}Fe_{0.2}Mn_{0.2}Ti_{0.2}O_2$	2-4.2	145.7	471.6	3.24	29
	$Na_{2/3}Ni_{1/3}Mn_{2/3}O_2$	1.5-4.5	158.2	565.4	3.58	30
	$Na_{0.8}Li_{0.12}Ni_{0.22}Mn_{0.66}O_2$	2.0-4.4	117.3	389.6	3.23	31
	$Na_{0.67}Mn_{0.8}Mg_{0.2}O_2$	1.5-4.0	128.3	352.8	2.77	32
	$Na_{0.6}(Li_{0.2}Mn_{0.8})O_2$	2.0-4.5	160.7	498.5	3.12	33
	$Na_{0.67}Cu_{0.28}Mn_{0.72}O_2$	2.0-4.5	104.3	382.2	3.6	34
	$Na_{0.9}Cu_{0.22}Fe_{0.30}Mn_{0.48}O_2$	2.0-4.0	100.8	319.3	3.2	35
	$Na_{0.75}Li_{0.25}Mn_{0.75}O_2$ @10%mol $Na_{0.44}MnO_2$	1.5-4.4	246.6	635.6	2.8	**This work**

Table S6. Contact angle result of the NLMO cathode material.

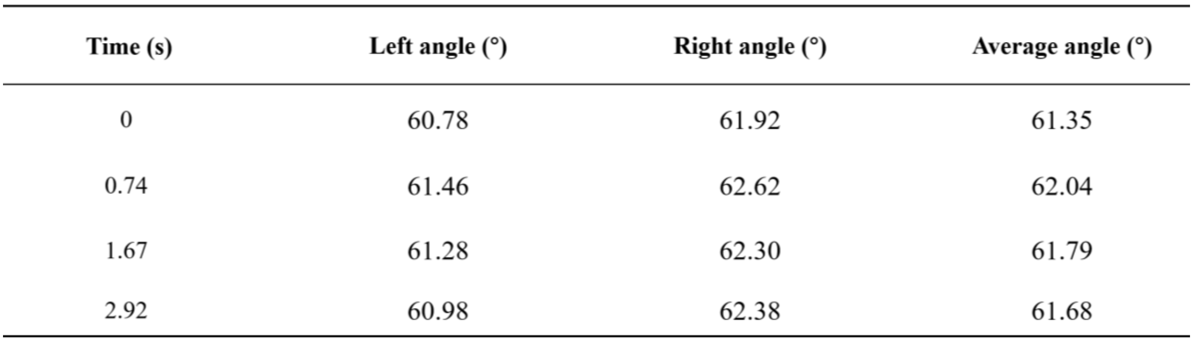

Time (s)	Left angle (°)	Right angle (°)	Average angle (°)
0	60.78	61.92	61.35
0.74	61.46	62.62	62.04
1.67	61.28	62.30	61.79
2.92	60.98	62.38	61.68

Table S7. Contact angle result of the NLMO-T10 cathode material.

Time (s)	Left angle (°)	Right angle (°)	Average angle (°)
0	115.23	114.25	114.74
0.74	115.67	114.85	115.26
1.67	116.08	114.78	115.43
2.92	116.24	114.02	115.13

Table S8. Zeta electric potential results of NLMO, NLMO-T05, NLMO-T10 and NLMO-T15 cathode materials.

Sample	Zeta electric potential (mV)
NLMO	-62.1
NLMO-T05	-101.2
NLMO-T10	-50.9
NLMO-T15	-89.1

Note S1. Na^+ Diffusion Coefficients Calculation Based on CV Measurements

The Na^+ diffusion coefficients (D Na^+) can be determined based on the CV results at various sweep rates according to the Randles-Sevcik formula: $i_p = (2.69\times10^5)n^{3/2}SD_{Na+}{}^{1/2}C_{Na}v^{1/2}$, where i_p is the peak current, n is the number of transferred electron number per molecule, Sis contact area between electrode and electrolyte (0.785 cm^2), C_{Na} is the Na^+ concentration in the electrode, and v is the scan rate. Therefore, the peak current i_p is directly proportional to the square root of the scan rate ($v^{1/2}$). The D Na^+ can be qualitatively assessed by establishing a linear relationship between the two variables and comparing their slopes, that is, a larger slope indicates a higher diffusion coefficient.

Note S2. Na$^+$ Diffusion Coefficients Calculation Based on GITT Measurements

The cell was charged or discharged at 0.1 C for 30 min and then relaxed for 600 min to allow the voltage to reach equilibrium. The Na$^+$ diffusion coefficients (D Na$^+$) can be calculated based on the simplified equation:

$$D = \frac{4}{\pi\tau}\left(\frac{m_B V_M}{M_B A}\right)^2 \left(\frac{\Delta E_S}{\Delta E_\tau}\right)^2 \quad \left(\tau \ll \frac{L^2}{D}\right) \quad \text{(S1)}$$

Where τ is the duration time of the current pulse, M_B is the molecular weight (g mol^{-1}), m_B is the mass of the active material, V_M is the molar volume (cm^3 mol^{-1}), A is the total contact area between electrode and electrolyte, ΔE_S is the difference between two consecutive stable voltages at the end of the relaxation period, $\Delta E\tau$ is the potential difference between the equilibrium potential and the potential maximum at the end of the current pulse, and L is the thickness of the working electrode (≈100 μm in the present study).

Equation S1. Calculation method for control equations in mechanical stress simulation based on COMSOL

(a) Formula for calculating principal stress and various stress matrix operations based on this calculation.

$I_1 = \sigma_{xx} + \sigma_{yy} + \sigma_{zz}$

$I_2 = \sigma_{xx}\sigma_{yy} + \sigma_{yy}\sigma_{zz} + \sigma_{zz}\sigma_{xx} - \sigma^2_{xy} - \sigma^2_{yz} - \sigma^2_{zx}$

$$I_3 = \sigma_{xx}\sigma_{yy}\sigma_{zz} - \sigma_{xx}\sigma^2_{yz} + \sigma_{zz}\sigma_{xx} - \sigma_{xy}^2 - \sigma_{yz}^2 - \sigma_{zx}^2 \sigma = \begin{pmatrix} \sigma_x & \tau_{xy} & \tau_{xz} \\ \tau_{yx} & \sigma_y & \tau_{yz} \\ \tau_{zx} & \tau_{zy} & \sigma_z \end{pmatrix} =$$

$$\begin{pmatrix} \sigma_{11} & \sigma_{12} & \sigma_{13} \\ \sigma_{21} & \sigma_{22} & \sigma_{23} \\ \sigma_{31} & \sigma_{32} & \sigma_{33} \end{pmatrix} = A \begin{pmatrix} \sigma_1 & 0 & 0 \\ 0 & \sigma_2 & 0 \\ 0 & 0 & \sigma_3 \end{pmatrix} A^{-1}$$

$\sigma_1 \geq \sigma_2 \geq \sigma_3$

Tresca stress: $\sigma_1 - \sigma_3 \leq [\sigma]$

von Mises stress: $\sqrt{0.5 * [(\sigma_1 - \sigma_2)^2 + [(\sigma_1 - \sigma_3)^2 + [(\sigma_2 - \sigma_3)^2\ ]} \leq [\sigma]$

(b) Relationship between deformation displacement and strain.

$$\boldsymbol{\varepsilon} = \frac{\mathbf{1}}{\mathbf{2}}((\nabla \cdot \boldsymbol{u})^{\boldsymbol{T}} + \nabla \cdot \boldsymbol{u})$$

(c) Generalized *Hooke's* Law in Matrix Form. For an anisotropic linear elastic material, the constitutive relationship between stress and strain can be expressed in matrix notation as:

$$\begin{bmatrix} \sigma_{11} \\ \sigma_{22} \\ \sigma_{33} \\ \tau_{12} \\ \tau_{23} \\ \tau_{31} \end{bmatrix} = \begin{bmatrix} C_{11} & C_{12} & C_{13} & C_{14} & C_{15} & C_{16} \\ C_{21} & C_{22} & C_{23} & C_{24} & C_{25} & C_{26} \\ C_{31} & C_{32} & C_{33} & C_{34} & C_{35} & C_{36} \\ C_{41} & C_{42} & C_{43} & C_{44} & C_{45} & C_{46} \\ C_{51} & C_{52} & C_{53} & C_{54} & C_{55} & C_{56} \\ C_{61} & C_{62} & C_{63} & C_{64} & C_{65} & C_{66} \end{bmatrix} \begin{bmatrix} \varepsilon_{11} \\ \varepsilon_{22} \\ \varepsilon_{33} \\ \varepsilon_{12} \\ \varepsilon_{23} \\ \varepsilon_{31} \end{bmatrix}$$

(d) The major governing equations used in the model.

Process	**Governing equation**
In Electrolyte	
Electrolyte Current flow	$i_l = -\sigma_l \nabla \phi_l + \frac{2\sigma_l RT}{F}(1 - t_+)\nabla \ln c_l$
Mass balance	$\frac{\partial c_l}{\partial t} + \nabla \cdot \left(-D_l \nabla c_l + \frac{i_l t_+}{F}\right) = 0$
Effective diffusion coefficient	$D_{m,eff} = {\epsilon_{l,m}}^{1.5} D_m$
Solid charge balance	$\nabla \cdot (-\sigma_s \nabla \phi_s) = 0$

Overpotential $\eta_m = \phi_s - \phi_l - E_{eq,m}$

In P2 bulk

Interfacial reaction
$$\boldsymbol{i_{P2} = i_{0,bulk}\left(\exp\left(\frac{\alpha F\eta}{RT}\right) - \exp\left(\frac{-(1-\alpha)F\eta}{RT}\right)\right)}$$

$$\boldsymbol{i_0 = Fk_{bulk}c_{P2,surf}{}^{0.5}\left(c_{bulk,max} - c_{bulk,surf}\right)^{0.5}\left(\frac{c_l}{c_{ref}}\right)^{0.5}}$$

Charge balance $\nabla \cdot (-\sigma_s \nabla \phi_s) = -A_v i_{bulk}$

Specific surface area
$$A_v = \frac{3}{r_p}$$

Mass balance
$$\frac{\partial \epsilon_{\mathrm{l,bulk}} c_{\mathrm{l}}}{\partial \mathrm{t}} + \nabla \cdot \left(-D_{l,eff}\nabla c_l + \frac{i_l t_+}{F}\right) = \frac{A_v i_{bulk}}{F}$$

Diffusion within solid phase
$$\frac{\partial c_{bulk}}{\partial t} = \frac{1}{r^2}\frac{\partial}{\partial r}\left(r^2 \frac{\partial c_{bulk}}{\partial r}\right)$$

In P2 bulk/ Tunnel coating

Interfacial reaction
$$\boldsymbol{i_{bulk/coating} = i_{0,bulk/coating}\left(\exp\left(\frac{\alpha F\eta}{RT}\right) - \exp\left(\frac{-(1-\alpha)F\eta}{RT}\right)\right)}$$

$$\boldsymbol{i_0 = Fk_{bulk/coating}c_{bulk/coating,surf}{}^{0.5}\left(c_{bulk/coating,max} - c_{bulk/coating,surf}\right)^{0.5}\left(\frac{c_l}{c_{ref}}\right)^{0.5}}$$

Charge balance $\nabla \cdot (-\sigma_s \nabla \phi_s) = -A_v i_{si}$

Specific surface area
$$A_v = \frac{3}{r_p}$$

Mass balance
$$\frac{\partial \epsilon_{\mathrm{l,si}} c_{\mathrm{l}}}{\partial \mathrm{t}} + \nabla \cdot \left(-D_{l,eff}\nabla c_l + \frac{i_l t_+}{F}\right) = \frac{A_v i_{si}}{F}$$

Diffusion within solid phase
$$\frac{\partial c_{si}}{\partial t} = \frac{1}{r^2}\frac{\partial}{\partial r}\left(r^2 \frac{\partial c_{si}}{\partial r}\right)$$

The calculation methods for *von Mises* stress and *Tresca* stress are shown in Eq. S1a. The relationship between deformation displacement and strain is explicitly defined in Eq. S1b, while the stress-strain relationships are governed by the generalized *Hooke's* law Eq. S1c. This multiscale framework constitutes the core coupling mechanism that links electrochemical processes to mechanical stress generation. To further support the COMSOL calculation results, we have added relevant content to Eq. S1d that supports information.

References

1. P. Barpanda, G. Oyama, S. Nishimura, S. C. Chung and A. Yamada, *Nat. Commun.*, 2014, **5**, 4358.
2. P. K. Dwivedi, S. K. Sapra, J. Pati and R. S. Dhaka, *ACS Appl. Energy Mater.*, 2021, **4**, 8076-8084.
3. T. Or, K. Kaliyappan, G. Li, S. Abureden, Z. Bai and Z. Chen, *Electrochim. Acta*, 2020, **342**, 136024.
4. X. Shen, J. Zhao, Y. Li, X. Sun, C. Yang, H. Liu and Y.-S. Hu, *ACS Appl. Energy Mater.*, 2019, **2**, 7474-7482.
5. L. Lei, K. Sun, Z. Hongwei, C. Wang and T. Wei, *J. Energy Storage*, 2024, **78**, 109923.
6. P. Barpanda, T. Ye, M. Avdeev, S.-C. Chung and A. Yamada, *J. Mater. Chem. A*, 2013, **1**, 4194.
7. Y. Zhu, H. Xu, J. Ma, P. Chen and Y. Chen, *J. Solid State Chem.*, 2023, **317**, 123669.
8. H. Li, T. Wang, S. Wang, X. Wang, Y. Xie, J. Hu, Y. Lai and Z. Zhang, *ACS Sustainable Chem. Eng.*, 2021, **9**, 11798-11806.
9. P. Singh, K. Shiva, H. Celio and J. B. Goodenough, *Energy & Environ. Sci.*, 2015, **8**, 3000-3005.
10. H. Liao, Z. Zhang, Y. Zheng and Y. Gao, *Energy Storage Mater.*, 2024, **65**, 103157.
11. D. Yang, X.-Z. Liao, B. Huang, J. Shen, Y.-S. He and Z.-F. Ma, *J. Mater. Chem. A*, 2013, **1**, 13417.
12. Z. Li, Y. Wang, F. Rabuel, M. Deschamps, G. Rousse, O. Sel and J.-M. Tarascon, *Energy Storage Mater.*, 2025, **76**, 104118.
13. F. Peng, L. Yu, P. Gao, X.-Z. Liao, J. Wen, Y.-s. He, G. Tan, Y. Ren and Z.-F. Ma, *J. Mater. Chem. A*, 2019, **7**, 22248-22256.
14. C. M. Kareis, S. H. Lapidus, J.-H. Her, P. W. Stephens and J. S. Miller, *J. Am. Chem. Soc.*, 2012, **134**, 2246-2254.
15. Y. Li, Z. Yang, S. Xu, L. Mu, L. Gu, Y. S. Hu, H. Li and L. Chen, *Adv. Sci.*, 2015, **2**.
16. N. Sabi, S. Doubaji, K. Hashimoto, S. Komaba, K. Amine, A. Solhy, B. Manoun, E. Bilal and I. Saadoune, *J. Power Sources*, 2017, **342**, 998-1005.
17. J. Ma, S.-H. Bo, L. Wu, Y. Zhu, C. P. Grey and P. G. Khalifah, *Chem. Mater.*, 2015, **27**, 2387-2399.
18. Y. Wang, J. Liu, B. Lee, R. Qiao, Z. Yang, S. Xu, X. Yu, L. Gu, Y. S. Hu, W. Yang, K. Kang, H. Li, X. Q. Yang, L. Chen and X. Huang, *Nat. Commun.*, 2015, **6**, 6401.

19. H. Liu, L. Kong, H. Wang, J. Li, J. Wang, Y. Zhu, H. Li, Z. Jian, X. Jia, Y. Su, S. Zhang, J. Mao, S. Chen, Y. Liu, S. Chou and Y. Xiao, *Adv. Mater.*, 2024, **36**, 2407994.
20. M. Jeong, H. Lee, J. Yoon and W.-S. Yoon, *J. Power Sources*, 2019, **439**, 227064.
21. M. A. Khan, D. Han, G. Lee, Y.-I. Kim and Y.-M. Kang, *J. Alloys Compd.*, 2019, **771**, 987-993.
22. N. Yabuuchi, M. Yano, H. Yoshida, S. Kuze and S. Komaba, *J. Electrochem. Soc.*, 2013, **160**, A3131-A3137.
23. S. Kalluri, K. H. Seng, W. K. Pang, Z. Guo, Z. Chen, H.-K. Liu and S. X. Dou, *ACS Appl. Mater. Interfaces*, 2014, **6**, 8953-8958.
24. Z.-C. Jian, Y.-F. Liu, Y.-F. Zhu, J.-Y. Li, H.-Y. Hu, J. Wang, L.-Y. Kong, X.-B. Jia, H.-X. Liu, J.-X. Guo, M.-Y. Li, Y.-S. Xu, J.-F. Mao, S.-L. Zhang, Y. Su, S.-X. Dou, S.-L. Chou and Y. Xiao, *Nano Energy*, 2024, **125**, 109528.
25. U. Maitra, R. A. House, J. W. Somerville, N. Tapia-Ruiz, J. G. Lozano, N. Guerrini, R. Hao, K. Luo, L. Jin, M. A. Pérez-Osorio, F. Massel, D. M. Pickup, S. Ramos, X. Lu, D. E. McNally, A. V. Chadwick, F. Giustino, T. Schmitt, L. C. Duda, M. R. Roberts and P. G. Bruce, *Nat. Chem.*, 2018, **10**, 288-295.
26. M. H. Han, E. Gonzalo, N. Sharma, J. M. López del Amo, M. Armand, M. Avdeev, J. J. Saiz Garitaonandia and T. Rojo, *Chem. Mater.*, 2015, **28**, 106-116.
27. Y. Huang, Y. Zhu, A. Nie, H. Fu, Z. Hu, X. Sun, S. C. Haw, J. M. Chen, T. S. Chan, S. Yu, G. Sun, G. Jiang, J. Han, W. Luo and Y. Huang, *Adv. Mater.*, 2022, **34**, 2105404.
28. H. Yoshida, N. Yabuuchi, K. Kubota, I. Ikeuchi, A. Garsuch, M. Schulz-Dobrick and S. Komaba, *Chem. Commun.*, 2014, **50**, 3677-3680.
29. X. Sun, Y. Jin, C.-Y. Zhang, J.-W. Wen, Y. Shao, Y. Zang and C.-H. Chen, *J. Mater. Chem. A*, 2014, **2**, 17268-17271.
30. Q. Liu, Z. Hu, M. Chen, C. Zou, H. Jin, S. Wang, Q. Gu and S. Chou, *J. Mater. Chem. A*, 2019, **7**, 9215-9221.
31. J. Xu, D. H. Lee, R. J. Clément, X. Yu, M. Leskes, A. J. Pell, G. Pintacuda, X.-Q. Yang, C. P. Grey and Y. S. Meng, *Chem. Mater.*, 2014, **26**, 1260-1269.
32. N. Sharma, N. Tapia-Ruiz, G. Singh, A. R. Armstrong, J. C. Pramudita, H. E. A. Brand, J. Billaud, P. G. Bruce and T. Rojo, *Chem. Mater.*, 2015, **27**, 6976-6986.
33. K. Du, J. Zhu, G. Hu, H. Gao, Y. Li and J. B. Goodenough, *Energy & Environ. Sci.*, 2016, **9**, 2575-2577.
34. W. Zheng, Q. Liu, Z. Wang, Z. Wu, S. Gu, L. Cao, K. Zhang, J. Fransaer and Z. Lu, *Energy Storage Mater.*, 2020, **28**, 300-306.

35. W. Zhang, Y. Zhang, J. Zhou, X. Li, W. Zhou, D. Zhang, J. Mao and K. Dai, *J. Electrochem. Soc.*, 2023, **170**, 070518.